Electronic Supplementary Information for

Solar-driven H_2O_2 production via cooperative auto- and photocatalytic oxidation in fine-tuned reaction media

Byeong Cheul Moon[a,1], Bolormaa Bayarkhuu[b,c,1], Kai A. I. Zhang[d], Dong Ki Lee[a,c,e,f*], Jeehye Byun[b,c*]

[a]Clean Energy Research Center, Korea Institute of Science and Technology, Seoul 02792, Republic of Korea
[b]Water Cycle Research Center, Korea Institute of Science and Technology, Seoul 02792, Republic of Korea
[c]Division of Energy and Environment Technology, KIST-School, University of Science and Technology, Seoul 02792, Republic of Korea
[d]Department of Materials Science, Fudan University, Shanghai 200433, People's Republic of China
[e]Graduate School of Energy and Environment, Korea University, Seoul 02841, Republic of Korea
[f]Department of Chemical and Biomolecular Engineering, Yonsei-KIST Convergence Research Institute, Yonsei University, Seoul 03722, Republic of Korea
[1]Equally contributed
*Corresponding authors: D. K. Lee (dnklee@kist.re.kr), J. Byun (jbyun@kist.re.kr)

Methods

Materials

All the chemicals and solvents were used without purification otherwise noted. 1,4-Dicyanobenzene (98%), (1,1'-biphenyl)-4,4'-dicarbonitrile (98%), tetrabutylammonium hexafluorophosphate ($TBAPF_6$, 98%), 4-fluorobenzyl alcohol (98%), 4-methylbenzyl alcohol (98%), graphitic carbon nitride (g-C_3N_4, 95%), 5,5-dimethyl-1-pyrroline-N-oxide (DMPO), anhydrous magnesium sulfate (98%), and α-methylbenzyl alcohol (99%) were purchased from TCI Korea. Titanium sulfate solution (24%) was obtained from Kanto chemicals. Thiophene-2,5-dicarbonitrile (98%) was supplied by BLD Pharmatech. Hydrogen peroxide (30 wt% in water), sodium hydroxide (98%), isopropyl alcohol (IPA, 99%), silver nitrate (99%), cerium(IV) sulfate, α,α,α-trifluorotoluene (TFT, 98%), BzOH (>99%), acetonitrile anhydrous (99.8%), diphenylmethanol (99.8%), nafion perfluorinated resin solution, and iron(II) sulfate heptahydrate (>99%) were purchased from Sigma-Aldrich. P25 titanium dioxide was obtained from Degussa (Evonik). BzOH-d_7 (98%) was supplied from Cambridge Isotope Laboratories, Inc. Trifluoromethanesulfonic acid (TfOH, 98%) was purchased from Acros Organics. Polystyrene latex microsphere (0.75 micron, 2 wt% dispersion in water) was supplied from Alfa-Aesar. Water was used in Millipore quality (< 18.2 MΩ cm).

Synthesis of CTF photocatalyst

CTF-Ph was prepared via solid-phase polymerization of aryl nitriles as reported elsewhere[1]. Dicyanobenzene monomer (200 mg) was placed in a 25 mL Schlenk tube in which a small glass vial (2 mL size) was placed including TfOH (0.3 mL). The Schlenk tube was degassed with Ar and the polymerization reaction took place for 24 h at 100 ^{o}C. After cooling to room temperature, the collected sample was washed with water, diluted ammonium hydroxide solution, excess water, and acetone followed by drying in the oven at 80 ^{o}C for overnight. The obtained sample was ground in a mortar and washed with ethanol. After collecting the powder by centrifugation, the polymer photocatalyst was obtained with a yield of 80-95%.

Characterizations

^{1}H NMR spectra were obtained by a Bruker Avance 400 MHz NMR spectrometer. Solid-state ^{13}C cross-polarization magic angle spinning (CP-MAS) NMR spectra were recorded on a Varian Solid 400 MHz NMR Premium Shielded & console spectrometer. Solid-state diffuse reflectance UV-vis spectra and UV-vis absorption spectra of liquid samples were taken from a Scinco S-3100 spectrophotometer. Photoluminescence (PL) spectra of polymer dispersion were collected by a Shimadzu F6000 spectrofluorophotometer. For PL measurement, the polymer was dispersed in the water/organic mixture and stirred overnight to make a fine dispersion. Time-resolved photoluminescence (TRPL) spectra of polymer dispersion were obtained by a Horiba

Fluorolog3 equipped with a pulsed laser diode 374 nm and a single photon counting PMT detector. Surface areas were measured by nitrogen adsorption-desorption at 77 K using a Micromeritics Triflex accelerated surface area and porosimetry analyzer. X-ray photoelectron spectroscopy (XPS) analysis was performed with Thermo Fisher Scientific Nexsa equipped with a microfocus monochromatic Al-Kα source. Beam spot size was 400 µm x 400 µm and a dual neutralizer (Argon ion + electrons) was used. The obtained XPS spectra were fitted using CasaXPS, where the C (1s) line for adventitious carbon was found at 284.8 eV. Powder X-ray diffraction (PXRD) patterns were recorded over the 2θ range of 10-90^{o} using a Bruker D8 ADVANCE model. Fourier-transform infrared spectroscopy (FT-IR) measurement was conducted with a Thermo scientific NICOLET iS10 with a KBr/Ge mid-infrared beam splitter. Gas chromatography mass spectrometry (GC-MS) was carried out using a LECO Pegasus IV instrument with an auto-sampler on a capillary column (DB-5ms; length, 30 m; inner diameter, 0.25 mm; column film 0.25µm), using helium as carrier gas at a flow rate of 0.8 ml min^{-1}. A temperature program of an initial isothermal step of 5 min at 50 °C, followed by heating at 20 °C min^{-1} to 280 °C with 5 min. The injector temperature was 300 °C and a transfer line temperature of 280 °C. The surface morphology of photoelectrode was performed with field emission-scanning electron microscopy (FE-SEM, Hitachi, Regulus8230, Japan) with an accelerating voltage of 15 kV. Total organic carbon (TOC) content was determined by using a Shimadzu TOC-L analyzer.

Photocatalytic production of H_2O_2 and BzCHO in designed OWSs

In a typical experiment, the CTF photocatalyst (50 mg) was dispersed in OWS (30 mL) and the suspension was transferred to a photo-reactor with a quartz cover (diameter = 10 cm, thickness= 1 mm) and purged with O_2 for 30 min in dark before reaction (**Fig. S31**). Photocatalytic reaction was conducted by stirring under the oxygen-saturated condition for 3 h irradiation, where the reaction mixture was irradiated with AM 1.5G simulated sunlight using a solar simulator (ABET technologies, Sun 3000 Class AAA, USA) equipped with 300 W DC xenon arc lamp. The incident light intensity was detected using a TES-132 Solar Power Meter. The concentration of H_2O_2 was colorimetrically determined by UV-vis spectroscopy and that of BzCHO was analysis by GCMS as described in the following sections.

Determination of H_2O_2 concentration

The obtained H_2O_2 concentration was measured by a titanium sulfate titration method[2]. Titanium sulfate solution (24%) was diluted into 0.64% in sulfuric acid solution (2 M). For the detection of H_2O_2 from the reaction in an aqueous solution or MeCN, the sample aliquot (1 mL) after the separation of CTF by micro-centrifugation was added with the titanium sulfate solution (0.1 mL). To detect the H_2O_2 concentration in non-polar TFT solvent, in contrast, H_2O_2 in the reaction solvent was extracted with

water and the extracted aqueous solution containing H_2O_2 was measured by titanium sulfate solution. A bright yellowish color was observed by the addition of titanium solution and the absorption peak at 405 nm was monitored by UV-vis spectroscopy. A calibration curve was obtained by using standard H_2O_2 solutions with known concentrations (**Fig. S32a**). The concentration of H_2O_2 was cross-checked by a cerium sulfate ($Ce(SO_4)_2$) titration method reported elsewhere[3]. In this titration method, $Ce(SO_4)_2$ solution with yellow color can be reduced by H_2O_2, resulting in the colorless Ce^{3+} solution (equation 1). Thus, the concentration of H_2O_2 was determined by measuring the absorbance of the $Ce(SO_4)_2$ solution before and after the addition of H_2O_2 by UV-vis spectroscopy (equation 2).

$$2Ce^{4+} + H_2O_2 \rightarrow 2Ce^{3+} + 2H^+ + O_2 \qquad (1)$$

$$C(H_2O_2) = 1/2 \times C(Ce^{4+}) \qquad (2)$$

where $C(H_2O_2)$ and $C(Ce^{4+})$ are the concentration of H_2O_2 and Ce^{4+}, respectively.

Typically, $Ce(SO_4)_2$ solution (1 mM) was prepared in 0.5 M sulfuric acid solution. For obtaining the calibration curve, H_2O_2 stock solutions were added to $Ce(SO_4)_2$ solution, and the color change was measured at 316 nm by UV-vis spectroscopy (**Fig. S32b**). The concentration of H_2O_2 samples was determined based on the linear relationship between the absorbance and the concentration of $Ce(SO_4)_2$.

Determination of BzCHO concentration

BzCHO concentration was determined by the GCMS with the sample aliquot from the reaction (~0.4 mL). The samples were extracted/diluted using TFT up to 200 times, dried over an anhydrous $MgSO_4$ to remove water, and filtered through a 0.22 um syringe filter. The diluted organic solutions were taken for the GCMS and the BzCHO concentration were determined based on the calibration curve. For the calibration curve, standard solutions of BzCHO were prepared in the concentrations of 0.3, 1, 2.5, 5, and 10 mM (**Fig. S33**).

Solar-to-chemical energy conversion efficiency (SCC) measurement

The SCC efficiency was determined by the photocatalytic reactions under an AM 1.5G solar simulator. The SCC efficiency was calculated by the following equation[4]:

$$\text{SCC efficiency (\%)} = \frac{\left[\Delta G\ for\ H_2O_2\ production\ (Jmol^{-1})\right]\left[H_2O_2\ formed\ (mol)\right]}{\left[Total\ input\ power(W)\right]\left[Reaction\ time\ (s)\right]} \times 100$$

Where ΔG is the free energy change of hydrogen peroxide (117 kJ mol^{-1}) and the average irradiance of the AM 1.5 solar light was 980.88 W m^{-2}. The irradiated area of the sample was 0.007088 m^2.

Extraction and purification of H_2O_2 from OWS

The obtained H_2O_2 from the long-term experiment was purified by consecutive extraction and separation processes. First, the crude reaction solution in TFT (40 mL) was placed in a separatory funnel and extracted with water (50 mL × 4). The combined crude aqueous solution was diluted into ~2 L to afford enough feed solution in the filtration setup. The collected aqueous layer was purified by a crossflow reverse osmosis (RO) filtration. Typically, a flat-sheet seawater reverse osmosis (RO) desalination membrane from DOW Filmtec (SW30XLE) was used. A custom-built crossflow RO setup with an effective membrane area of 20.0 cm^2 was employed for the filtration experiment. Prior to testing, the membrane was pre-compacted under 20 bar hydraulic pressure with DI water as the feed for 4 h. The filtration experiment was conducted at a crossflow velocity of 0.21 m s^{-1} and temperature of 25.0 ± 0.5°C. The obtained permeate and crude feed samples were collected after the system was equilibrated for 1 h. The purity of filtered solution was determined by measuring the organic contents using ^1H NMR and TOC analyzer. For ^1H NMR analysis, a 50 µL purified sample was added to 450 µL of CD_3CN.

EPR measurements

EPR spectra were obtained by EPR spectrometer (Jeol JES-FA 200 X-band, 9.45 GHz, JAPAN, **Fig. S34**). The measurement parameters were microwave power of 5 mW, magnetic field modulation of 0.3 mT, modulation frequency of 100 kHz, and sweep width of 10 mT. All the experiments were conducted at room temperature, and the reaction solution was placed in a 4 ml vial under irradiation. After photo-reaction, EPR spectra of supernatant liquid was measured after separating photocatalyst powders using microcentrifugation. DMPO was used as a spin trap molecule. The formation of radical during O_2 reduction with methanol as electron donor was monitored in the O_2-saturated reaction mixture containing 10 mg of photocatalyst and 20 µl of DMPO in 3 mL MeOH. The formation of radical during O_2 reduction in the OWS was monitored in the O_2-saturated reaction mixture containing 10 mg of photocatalyst and 20 µl of DMPO in the mixture of 1.5 ml of BzOH and 1.5 ml of MeCN. The formation of radical during BzOH oxidation was monitored in the air-exposed reaction mixture containing 10 mg of photocatalyst and 20 µl of DMPO in 3 mL BzOH. *In-situ* EPR experiments were performed to track the reaction intermediates in the OWS by a time-resolved manner. Radical intermediates generated during the reaction were analyzed with Jeol LC-11 flat glass capillary sample tube (capillary volume: 100 µL) under simulated AM 1.5G light irradiation using a 300W xenon arc lamp. 100 µl of aliquot was loaded in the capillary tube for *in-situ* measurement, and the reaction mixture was prepared by dispersing 0.67 mg of photocatalyst and 1.33 µl of DMPO in the mixture of 50 µl of BzOH and 50 µl of MeCN. The data were collected every 1 min for total 30 min, including 30 s of measurement and 20 s of processing time. Additionally, 5 mol% of water was added in the reaction mixture to reveal the effect of

water on the radical formation. Measured EPR spectra were further processed to correct the magnetic field using standard Mn^{2+} marker and analyzed by Easyspin software package[5] to calculate the hyperfine splitting constants of radical intermediates: hyperfine coupling constant (A) and hyperfine tensor (g). Time-resolved quantitative analysis on the radicals was conducted by double integration of EPR signals where the EPR signal is first derivative of electromagnetic absorption spectrum.

Photocatalytic evolution of H_2 and O_2

CTF photocatalyst (20 mg) was dispersed in 20 mL of water and the suspension was transferred to a gas-tight quartz glass reactor and purged with He for 30 min in dark before reaction. Photocatalytic reaction was conducted with AM 1.5G simulated sunlight using solar simulator (ABET technologies, Sun 2000 Class A, USA) equipped with 150 W DC xenon arc lamp, and the amount of H_2 and O_2 was quantified by Neofox optical oxygen sensor (Ocean Optics, Netherlands) and gas chromatography (Youngin Chromass, YL6500 GC, Korea) equipped with pulsed discharge detector (PDD) and molecular-sieve coated PLOT capillary column (HP-Molesieve, Agilent technologies, USA).

Preparation of CTF catalyst ink

For the (photo)electrochemical measurements using different types of electrode substrates, CTF catalyst ink was prepared by dispersing 5 mg of CTFs powder in the mixture of 200 μL of IPA, 50 μL of water, and 50 μL of nafion perfluorinated resin solution, and the catalyst ink was sonicated for 30 min before use.

Electrochemical O_2 reduction

Rotating disk electrode (RDE) experiment was conducted on the rotating ring disk electrode (RRDE) setup (RRDE-3A model 2325, ALS, Japan) in three-electrode configuration with a glassy carbon disk electrode of RDE as working electrode (WE), Pt wire as counter electrode (CE), and Ag wire as reference electrode (RE). Prior to measurement, RDE was polished on polishing pads using alumina slurries before use. Then, 8 μL aliquot of catalyst ink was dropped on a glassy carbon disk (0.196 cm^2), and the electrode was dried under atmospheric conditions. Linear sweep voltammetry (LSV) was performed in O_2-saturated electrolytes at a scan rate of 10 mV s^{-1}, and the rotating rate of the RDE was 1600 rpm. In an aqueous condition, LSV was conducted in 0.1 M potassium phosphate (KPi) buffer solution (pH 7.2), and Ag/AgCl (filled with 3M KCl) was used for RE. In an organic condition, LSV was conducted in MeCN with 0.1 M $TBAPF_6$ as supporting electrolyte and 0.1 M BzOH as hole scavenger, and Ag/Ag^+ (filled with MeCN with 0.1 M $TBAPF_6$ and 0.01 M $AgNO_3$) was used for RE. In the designed OWSs (**Table S3**), LSV was conducted in water-MeCN mixture with 0.1 M $LiClO_4$ as supporting electrolyte, and Ag/Ag^+ (filled with the same water-acetonitrile mixture and 0.01 M $AgNO_3$) was used for RE. The onset potential was measured at -

10 μA cm^{-2}, and O_2 reduction current (J_{OR}) was compared at -1.5V vs. Ag/Ag^+. H_2O_2 selectivity was evaluated by RRDE experiment in four-electrode configuration using additional Pt ring electrode as second working electrode. Constant potential of 1.2 V vs. RHE was applied on the Pt ring electrode to detect H_2O_2 generated on the disk electrode. H_2O_2 selectivity and average electron transfer number (n) were calculated using the equations:

$$Selectivity\ (\%) = 200 \times \left(I_{ring}/N\right)/\left(I_{disk} + I_{ring}/N\right);$$

$$n = 4 \times |I_{disk}|/\left(I_{disk} + I_{ring}/N\right);$$

where I_{ring} and I_{disk} is ring current and disk current of RRDE electrode, respectively, and N is collection efficiency of 0.35.

Preparation of photoelectrodes

For the photoelectrochemical measurement, photoelectrode was prepared by following literature[6]. Briefly, fluorine-doped tin oxide (FTO) glass (1 x 3 cm^2) was sonicated in water, ethanol, and acetone for 15 min and dried with an air gun. Indium-tin oxide (ITO) nanoparticle dispersion (20 wt% in water, Aldrich) was diluted with IPA and sonicated for 30 min. Then, mesoporous ITO (mesoITO) electrode was prepared by drop-casting the ITO suspension on the FTO glass with controlled area (0.785 cm^2) by Parafilm as a spacer, and the electrode was dried under atmospheric conditions. Then, the mesoITO electrode was annealed in a box furnace at 450 ℃ for 20 min with an elevating rate of 4 ℃/min, and it was slowly cooled down to room temperature. Macroporous inverse opal structured ITO (IO-ITO) layer was also developed on the mesoITO layer to facilitate the loading of CTF catalysts on the electrode. To prepare IO-ITO layer, polystyrene beads solution was centrifuged at 6000 rpm for 15 minutes, and solution was decanted. Then, ITO suspension was mixed with polystyrene beads and sonicated for 30 minutes to prepare well-dispersed polystyrene/ITO suspension. IO-ITO/mesoITO electrode was then prepared by drop-casting of polystyrene/ITO suspension on the mesoITO layer with controlled area (0.785 cm^2) by Parafilm as a spacer, and the electrode was dried under atmospheric conditions. Then, the IO-ITO/mesoITO electrode was annealed in a box furnace at 450 ℃ for 90 min with an elevating rate of 4 ℃/min, and it was slowly cooled down to room temperature. Then, the photoelectrode was prepared by dropping 20 μL aliquot of the ink on the IO-ITO/mesoITO/FTO electrode, and the photoelectrode was dried at room temperature (**Fig. S35**).

Photoelectrochemical BzOH oxidation

All the measurements were conducted on the potentiostat (SP-240, Biologic, France) in three-electrode configuration with the CTF/IO-ITO/meso-ITO/FTO photoelectrode as WE, Pt wire as CE and Ag wire as RE. LSV was performed in Ar-saturated

electrolytes at a scan rate of 10 mV s^{-1} under AM 1.5G simulated sunlight using solar simulator. Photocurrent was measured using programmable light aperture with an interval of 5 s, and dark current of each photoelectrode was measured prior to performing LSVs. In an aqueous condition, LSV was conducted in 0.1 M KPi buffer solution (pH 7.2) with 0.1 M BzOH. Photocurrent for water oxidation was measured in 0.1 M KPi without BzOH. In an organic condition, LSV was conducted in MeCN with 0.1 M $TBAPF_6$ and 0.1 M BzOH. In the designed OWSs (**Table S3**), LSV was conducted in water-MeCN mixture with 0.1 M $LiClO_4$ and 0.1 M BzOH. The filling electrolyte for each RE was prepared in the same manner with the electrochemical O_2 reduction experiment. The onset potential was measured at 10 μA cm^{-2}, and alcohol oxidation photocurrent (J_{AO}) was compared at 2.0 V vs. Ag/Ag^+.

Table S1. Compositions of organic working solutions for solar H_2O_2 and benzaldehyde (BzCHO) production.

Molar ratio of water to BzOH %	H_2O weight %	H_2O, mL	BzOH, mL	Acetonitrile, mL
0	0	0	15	15
10	1	0.29	15	14.71
50	8.7	2.6	15	12.4
66	17.3	5.2	15	9.8
98.5	90	27	3	0

Table S2. A comparison of solar H_2O_2 production of CTF-Ph with state-of-the-art photocatalysts (PC) and electrocatalysts (EC).

Category	Material	Reaction conditions	H_2O_2	H_2O_2 production rate, μmol h^{-1} g_{cat}^{-1}	SCC efficiency (%)	Ref
PC	g-C_3N_4	O_2; 4 g/L (catalyst), 90 vol % of ethanol, Xe-lamp 420−500 nm, 26.9 W/m^2; 298 K	30 μmol for 12 h	125	N/A	7
	g-C_3N_4/PDI	O_2; 1.67 g/L (catalyst), in the pure water; λ>420 nm, 43.3 W/m^2; 298 K	14 μmol for 24 h	11.7	0.1	8
	g-C_3N_4/PDI/r$GO_{0.05}$	O_2; 1.67 g/L (catalyst), in the pure water; λ>420 nm, 43 W/m^2; 298 K	29 μmol for 24 h	24.17	0.2	8
	g-C_3N_4/PDIB$N_{0.2}$-r$GO_{0.05}$	O_2; 1.67 g/L (catalyst), in the pure water; λ>420 nm, 43.3 W/m^2; 298 K	37 μmol for 24 h	30.84	0.27	9
	Mesoporous g-C_3N_4	O_2; 4 g/L (catalyst), 90 vol % of ethanol, λ>420 nm, Xe-lamp, 26.9 W/m^2; 298 K	65 μmol for 24 h	135.4	N/A	10
	PEI/ C_3N_4	O_2; 1 g/L (catalyst), in pure water, AM 1.5, 100 mW /cm^2, 293K	208.1 μM for 1 h	208.1	0.045	11
	AQ-augmented g-C_3N_4	O_2; 0.5 g/L (catalyst), 10 vol % of isopropanol, AM 1.5, 100 mW/cm^2, 298 K	180.5 μM for 1 h	361	0.178	12
	Co_1/AQ/C_3	O_2; 0.5 g/L	62 μM	124	N/A	13

	N_4	(catalyst), in pure water, AM 1.5, 100 mW/cm^2, 298 K	for 1 h			
	C-N-g-C_3N_4	O_2; 0.9 g/L (catalyst), in pure water; 250 W lamp, 40 mW/m^2, 700>λ>420 nm; 298 K	11.76 μmol for 12 h	98	N/A	[14]
	BNQD/UPCN	O_2; 1 g/L (catalyst), 10 vol % of isopropanol in water; 300 W Xe-lamp λ>420nm; 298 K	72.3 μM for 1 h	72.3	N/A	[15]
	AQ/U-POCN	Air; 5 g/L (catalyst), in pure water, solar simulator with light intensity: 400-780 nm, 100 mW/cm^2, 298K	225 μM for 3 h	15	N/A	[16]
	OCN-500	O_2; 1 g/L (catalyst), 10 vol% of isopropanol in water (pH=7); Xe-lamp λ≥420nm, 35.2 mW/cm^2; 298K	730 μmol for 5 h	2920	N/A	[17]
	P-mMCNNS-25	O_2; 1.05 g/L (catalyst), 5 vol% of ethanol, AM 1.5, 100 mW/cm^2; 298 K	3249 μM for 3 h	1083	N/A	[18]
	Ni/MIL-125-NH_2	O_2; 1 g/L (catalyst), 20 vol% of benzyl alcohol in acetonitrile; Xe-lamp 500W, λ>420 nm; 298 K	7.5 mM for 8 h	937	N/A	[19]
	MIL-125-R7	O_2; 5 mg (catalyst), the two-phase system composed	2.4 mM for 3 h	800	N/A	[20]

		of benzyl alcohol (5.0 mL) and water (2.0 mL); Xe-lamp 500 W, λ≥420 nm; 298 K				
	OPA/$Zr_{92.5}Ti_{7.5}$-MOF	O_2; 5 mg (catalyst), the two-phase system composed of benzyl alcohol (5.0 mL) and water (2.0 mL); Xe-lamp 500 W, λ>420 nm; 298 K	29 mM for 3 h	9700	N/A	[21]
	Resorcinol – formaldehyde resins	O_2; 1.67 g/L (catalyst), in the pure water; Xe-lamp λ>420nm, 140.3 W/m^2; 333 K	99 μmol for 24 h	82.5	0.5	[22]
	CTF-BPDCN	O_2; 0.6 g/L (catalyst), in pure water; Xe-lamp 44.5 mW/m^2, λ≥420 nm; 298 K	21 μmol for 24 h	29.2	0.025	[3]
	CTF-EDDBN	O_2; 0.6 g/L (catalyst), in pure water; Xe-lamp 44.5 mW/m^2, λ≥420 nm; 298 K	39 μmol for 24 h	54.2	0.07	[3]
	CTF-BDDBN	O_2; 0.6 g/L (catalyst), in pure water; Xe-lamp 44.5 mW/m^2, λ≥420 nm; 298 K	70 μmol for 24 h	97.3	0.14	[3]
	TAPD-$(Me)_2$ COF	O_2; 4 g/L (catalyst), water:ethanol (1:9); 250 W lamp, 5.46 mW/m^2, 700≥λ≥420 nm; 298 K	57.2 μmol for 16 h	234.52	N/A	[23]
	PAE-D	O_2; 1 g/L (catalyst), 10 vol% isopropanol	51 μmol for 2 h	1275	N/A	[24]

		in water; 420 nm monochromatic LED lamp, 298 K				
	DE7-M	O_2; 1.67 g/L (catalyst), in pure water; 300 W Xe lamp with a filter λ>420 nm, 298 K	266 μmol for 24 h	221.7	0.28	[25]
	Nv-C≡N-CN	O_2; 1 g/L (catalyst), 10 vol% isopropanol in water; pH=3, AM 1.5G, 100 mW/cm^2, 298 K	3930 μmol for 1 h	3930	0.23	[26]
	AKMT	O_2; 0.5 g/L (catalyst), 10 vol% ethanol in water; pH=3, AM 1.5G, 298 K	3.41 mM for 1 h	6820	N/A	[27]
	Sb-SAPC15	O_2; 2 g/L (catalyst), in pure water; Xe lamp (light intensity at 420-500 nm, 30.3 Wm^{-2}) λ>420 nm, 298 K	470.5 μmol for 8 h	588.1	0.61	[28]
	PFBT-PCBM dots	O_2; 20 μg/ml (catalyst), 5 M methanol in 1 M KOH; pH=14, 50 mW/cm^2, 750≥λ≥420 nm; 298 K	5 mM for 80 min	188000	N/A	[29]
	$Co_2(OH)_2CO_3/Fe_3O_4/TiO_2$	O2; 0.1g/L (catalyst), in pure water; Xe-lamp 1000 W/m^2 , 298K	1.67 mmol for 1 h	1670	N/A	[30]
	CTF-Ph	O_2; 1.67g/L (catalyst), 50 vol% of benzyl alcohol in acetonitrile containing 0.96 wt%	7.04 mmol for 3 h	46933	1.097	**This work**

		of water; AM 1.5G, 980 W/m^2; 298 K				
EC*	Carbon black	O_2/SE/H_2; 0.46 mg/cm^2 (catalyst), 4 cm^2 MEA; O_2 flow rate 20 sccm, anolyte flow rate 2 mL/min, 298K	13.6 mmol for 1h	3400 μmol h^{-1} cm^{-2}	**	31
	Co_1-NG(O)	O_2/Selemion/0.1M KOH; 1 mg/cm^2 (catalyst), O_2 saturated, 298K	1.71 mmol for 24 h	418 μmol h^{-1} cm^{-2}	**	32
	Co-C	O_2/Nafion 112/H_2; 0.36 mg/cm^2 (catalyst), 49cm^2 MEA; O_2 flow rate 1000 mL/min, H_2 flow rate 500 mL/min, 333K	N/A	200 μmol h^{-1} cm^{-2}	**	33
	BP2000	O_2+H_2O/Nafion 117/SE/Nafion 117 /H_2O; O_2 flow rate 180 mL/min, H_2O flow rate 10.8 mL/min, 298K	30.9 mmol for 17 h	6520 μmol h^{-1} cm^{-2}	**	34
	H-Pd-OCNT	O_2+$HClO_4$/Nafion 117/0.1M $HClO_4$; O_2 saturated, 298K	N/A	170 μmol h^{-1} cm^{-2}	**	35

*H_2O_2 production rate of electrocatalysts is represented as a unit of μmol h^{-1} cm^{-2}_{geo} because the total mass of electrocatalysts is not provided in the literature.

**The SCC efficiency is omitted for electrocatalysts because the electrocatalytic systems are operated not by sunlight.

Table S3. Compositions for electrochemical evaluation of O_2 reduction and BzOH oxidation in the organic working solutions.

Volumetric ratio of water to acetonitrile, %	Molar ratio of water to BzOH, %	H_2O, mL	Acetonitrile, mL	BzOH, mL
0	0	0	40.00	0.42
0.01	5.01	0.003	39.996	0.42
0.02	10.00	0.006	39.992	0.42
0.14	50.00	0.054	39.60	0.42
0.27	66.67	0.108	39.20	0.42
5.00	97.37	2.000	38.00	0.42
10.0	98.67	4.000	36.00	0.42
50.0	99.73	20.00	20.00	0.42
66.6	99.80	26.66	13.34	0.42
98.5	99.86	39.40	0.600	0.42
100	99.87	40.00	0	0.42

Fig. S1. (a) The electronic band structures of CTF-Ph with a comparison of commercial P25 TiO_2. (b) The reduction potential of CTF-Ph and (c) TiO_2 determined by cyclic voltammetry (CV).

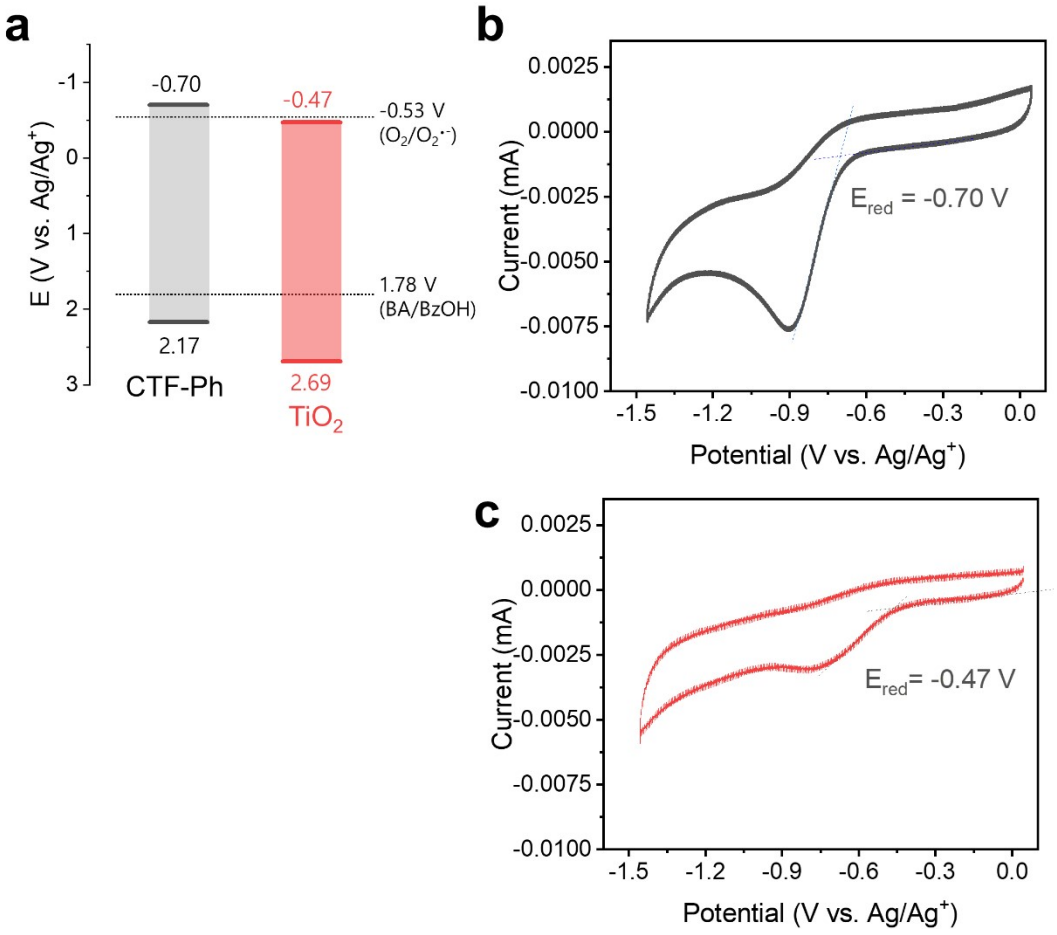

Note: CV revealed the reduction potentials of CTF-Ph and TiO_2 were located at -0.70 V and -0.47 V vs. Ag/Ag^+, respectively and the corresponding oxidation potentials were estimated to be 2.17 and 2.69 V vs. Ag/Ag^+ by subtracting the reduction potential from the optical band gap (2.87 eV for CTF-Ph and 3.15 eV for TiO_2), respectively.

Fig. S2. The frontier orbital distributions and the corresponding HOMO/LUMO values of (a) phenyl ring donor unit and (b) model structure of CTF-Ph, calculated at the B3LYP/6-31G(d) level.

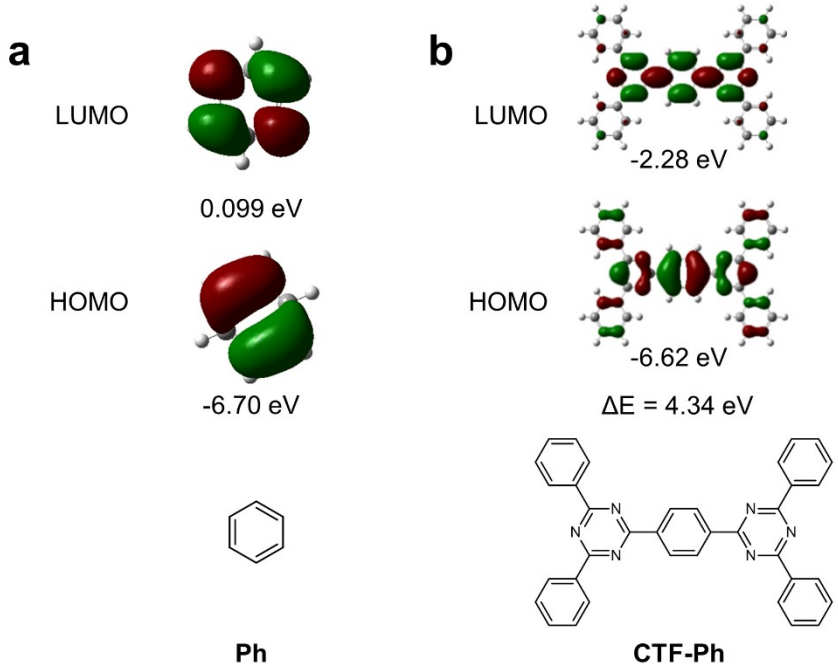

Fig. S3. (a) Solid-state ^{13}C CP-MAS NMR and (b) FT-IR spectrum of CTF-Ph.

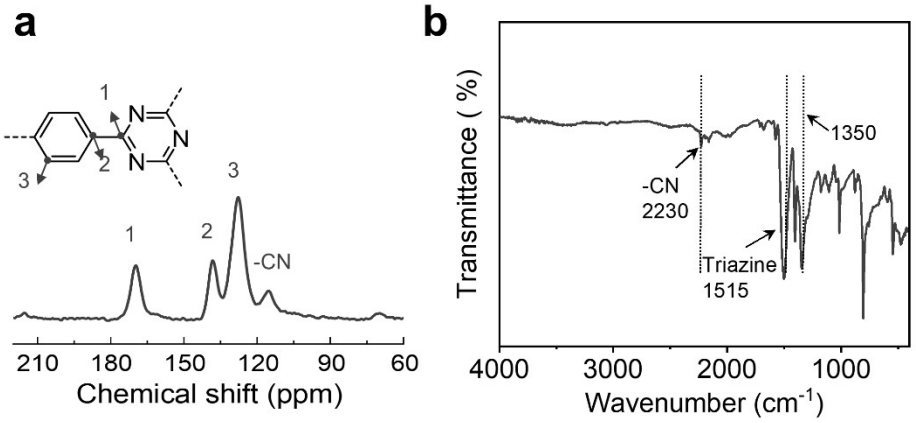

Note: (a) From ^{13}C CP-MAS solid-state NMR spectrum, the typical chemical shifts between 120 and 150 ppm shown for CTF-Ph originated from the aromatic rings as the donor site, corresponding to the previous report[1, 36]. A distinct peak at around 170 ppm in CTF-Ph was attributed to the sp^2-bonded carbon atoms in triazine rings as the acceptor site[3], indicating the successful trimerization of aryl nitriles. A small peak at 115 ppm was determined due to the unreacted terminal cyano groups[1]. (b) FT-IR spectrum showed two peaks at 1515 and 1350 cm^{-1} which are ascribed to the aromatic C-N stretching and breathing modes of triazine ring[3]. The slight peak at 2230 cm^{-1} indicates the cyano terminal group on the CTF-Ph.

Fig. S4. XPS (a) C 1s and (b) N 1s spectrum of CTF-Ph.

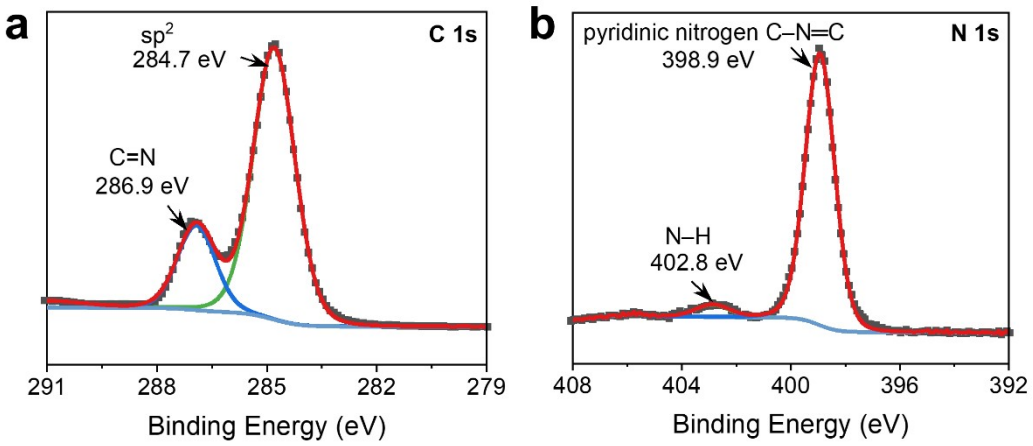

Note: (a) Two peaks at 284.7 eV and 286.9 eV are originated from sp^2 carbon in phenyl ring and C=N bond in triazine ring, respectively. (b) The dominant peak at 398.9 eV indicates the successful formation of pyridinic nitrogen (C-N=C) in triazine ring. The weak peak at 402.8 eV can be attributed to amine (N-H) formed by partial hydrolysis of nitrile in the strong TfOH[1].

Fig. S5. (a) N_2 adsorption-desorption isotherm of CTF-Ph at 77 K. (b) Powder X-ray diffraction (XRD) pattern of CTF-Ph.

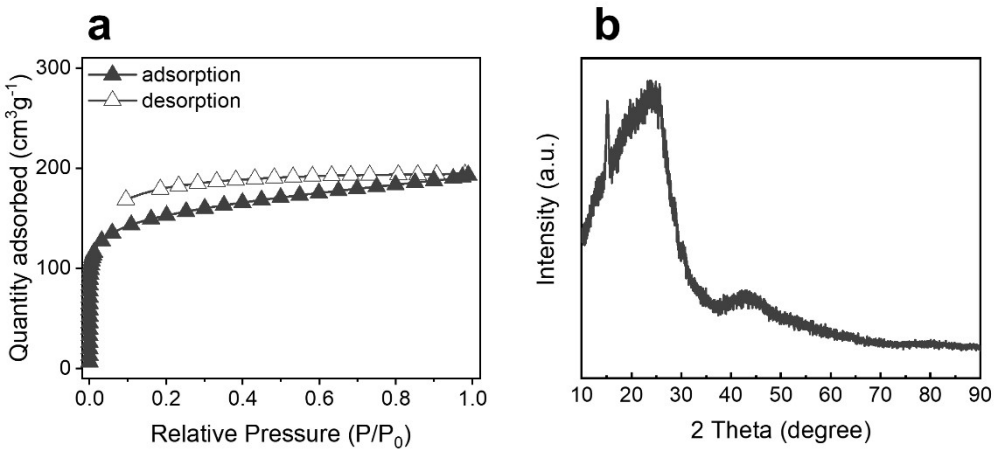

Note: (a) The measured Brunauer-Emmett-Teller (BET) surface area of CTF-Ph was 563.5 m^2 g^{-1}. (b) XRD pattern revealed that CTF-Ph is mainly an amorphous structure.

Fig. S6. Time-dependent photocatalytic production of (a) O_2 and H_2O_2, and (b) H_2 in pure water under an Ar-saturated condition using CTF-Ph photocatalyst.

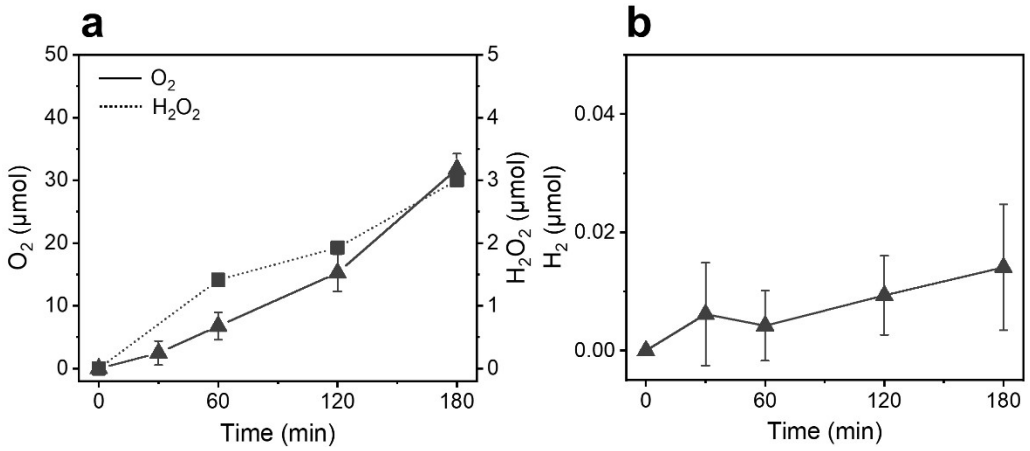

Note: (a) The strong oxidation potential of CTF-Ph led to a high O_2 production by water oxidation. Slight H_2O_2 formation was observed after 1 h of light treatment, indicating that O_2 formed by water oxidation contributed to the H_2O_2 production.

Fig. S7. J-V curves of CTF-Ph in Ar-saturated acetonitrile (0.1 M $TBAPF_6$) with 0.1 M BzOH.

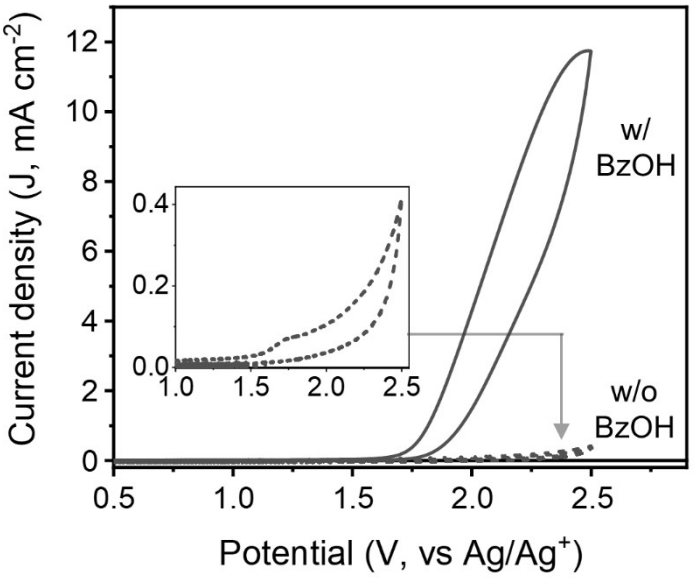

Fig. S8. H_2O_2 production during the photo-oxidation of various aryl alcohol substrates. Reaction conditions: aryl alcohol (5 mmol), CTF-Ph photocatalyst (15 mg), DMSO (5 mL), O_2 (1 bar), AM 1.5G simulated sunlight (~990 W m^{-2}), 298 K. Abbreviation: benzyl alcohol (BzOH), 4-fluorobenzyl alcohol (F-BzOH), 4-methylbenzyl alcohol (M-BzOH), α-methylbenzyl alcohol (α-M-BzOH), and diphenylmethanol (DPM).

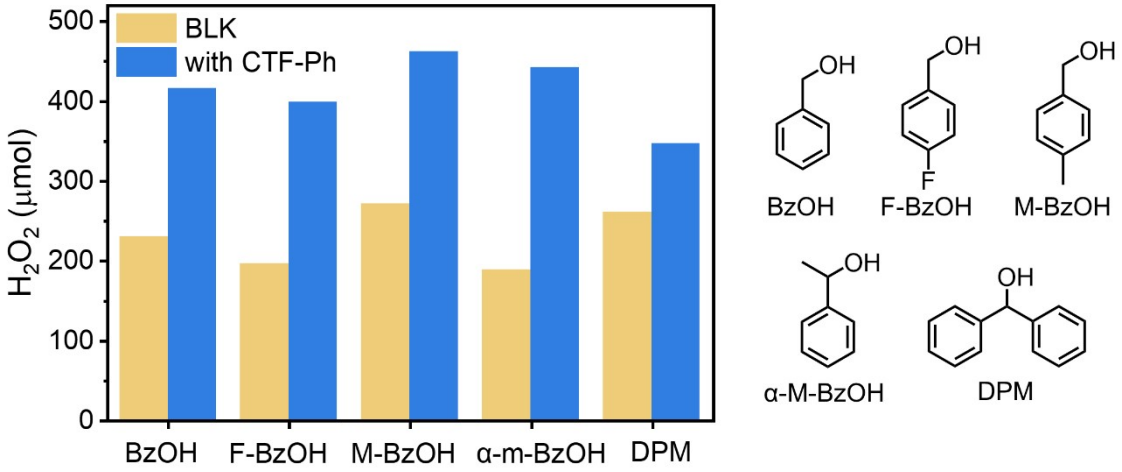

Note: DMSO was selected as a solvent in order to dissolve all the aryl alcohol substrates in identical solvent conditions. The lower H_2O_2 production shown in Fig. S8 than in Fig. 2 is because of low substrate loading and reaction scale. The tested aryl alcohol substrates produced a substantial amount of H_2O_2 even without the addition of a photocatalyst. The oxidized structure of those substrates exists from the beginning of the reaction (due to the partial oxidation of the substrates) and plays as the autocatalyst to form H_2O_2. That is, the excited triplet state of the aromatic aldehydes can abstract hydrogen from aryl alcohol as a hydrogen donor, making the α-hydroxylbenzyl radicals that can activate O_2 molecules.

Fig. S9. H_2O_2 selectivity and number of average electron transfer (n) during the LSV.

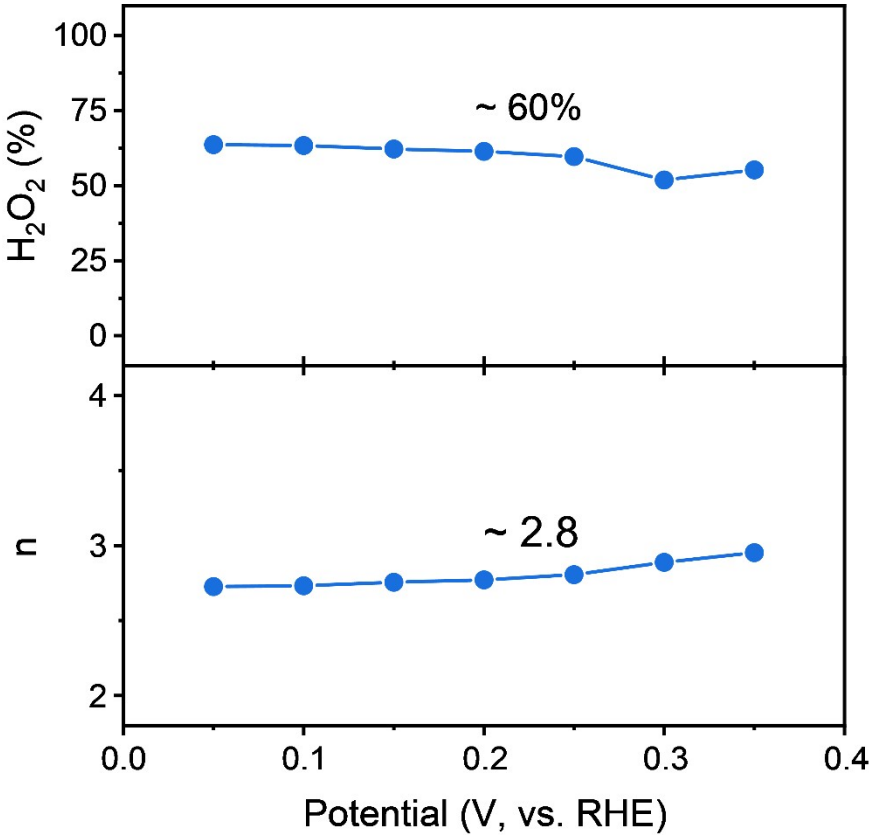

Note: The H_2O_2 selectivity (~60%) and the number of average electron transfer (~ 2.8) were calculated by equation described above in the method section for RRDE experiment.

Fig. S10. Photoelectrochemical oxidation of water in aqueous 0.1 M KPi with and without the addition of 0.1 M BzOH and 0.1M IPA under the simulated sunlight. BzOH oxidation current (gray) was also plotted for comparison.

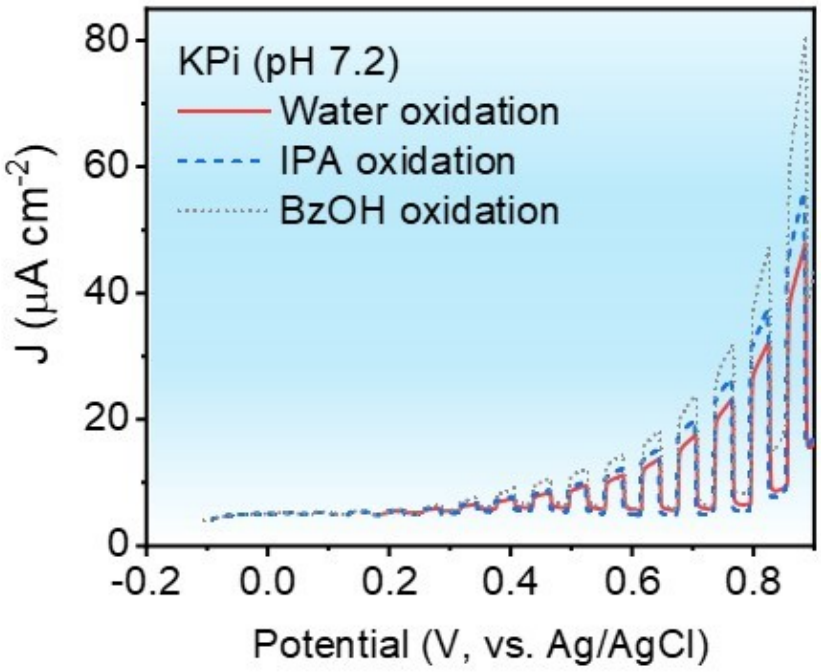

Note: Photocurrent from water oxidation is lower than that of BzOH oxidation, and the onset potential of water oxidation (0.2 V vs. Ag/AgCl) is higher than those of IPA or BzOH oxidation (-0.1 V vs. Ag/AgCl). With the addition of IPA, the photocurrent for IPA oxidation is higher than that of water oxidation (i.e. without a hole scavenger) but lower than that of BzOH oxidation. The hole scavenging efficiency from the photocatalyst depends on the redox potential of hole-trapping agents. The oxidation potential of BzOH (1.97 V vs. NHE) is close to that of CTF-Ph which is higher than that of IPA (-0.31 V vs. NHE). Higher redox potential facilitates efficient hole transport and hinders recombination of photogenerated electrons and holes in the photocatalysts,[37] thus BzOH gives higher oxidative photocurrent with higher H_2O_2 production in an aqueous condition.

Fig. S11. Light-dependent auto-catalytic production of (a) H_2O_2 and (b) BzCHO without addition of CTF-Ph in the organic condition. Reaction condition: organic working solution (50:50% BzOH:MeCN, 10 mL), O_2 (1 bar), 298 K, light variation using cut-off filters under a solar simulator (Newport, LHS300, ~990 W m^{-2}). For UV-A irradiation (315-400 nm), blacklight Blue UVA lamps (Philips, F4T5, Poland) were used with a peak emission wavelength of 352 nm.

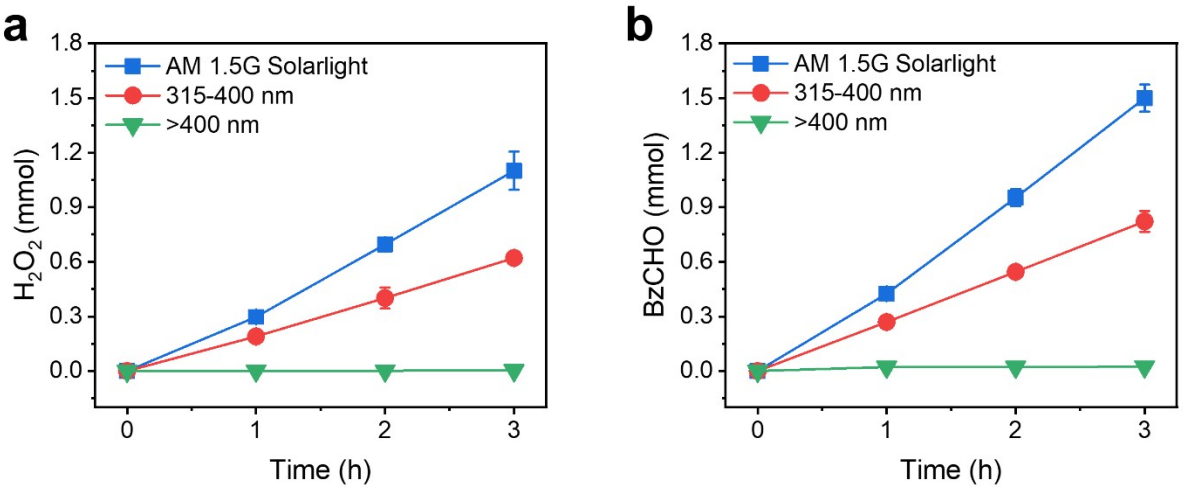

Fig. S12. (a) Detection of benzyl benzoate (BBA) side product in the organic working solutions. (b) Mass spectrum of the BBA taken from the GC-MS with a comparison of library match. Reaction condition: CTF-Ph (50 mg), organic working solutions (30 mL) with water content variations, AM 1.5G simulated sunlight (~990 W m^{-2}), 3 h, O_2 (1 bar), 298 K.

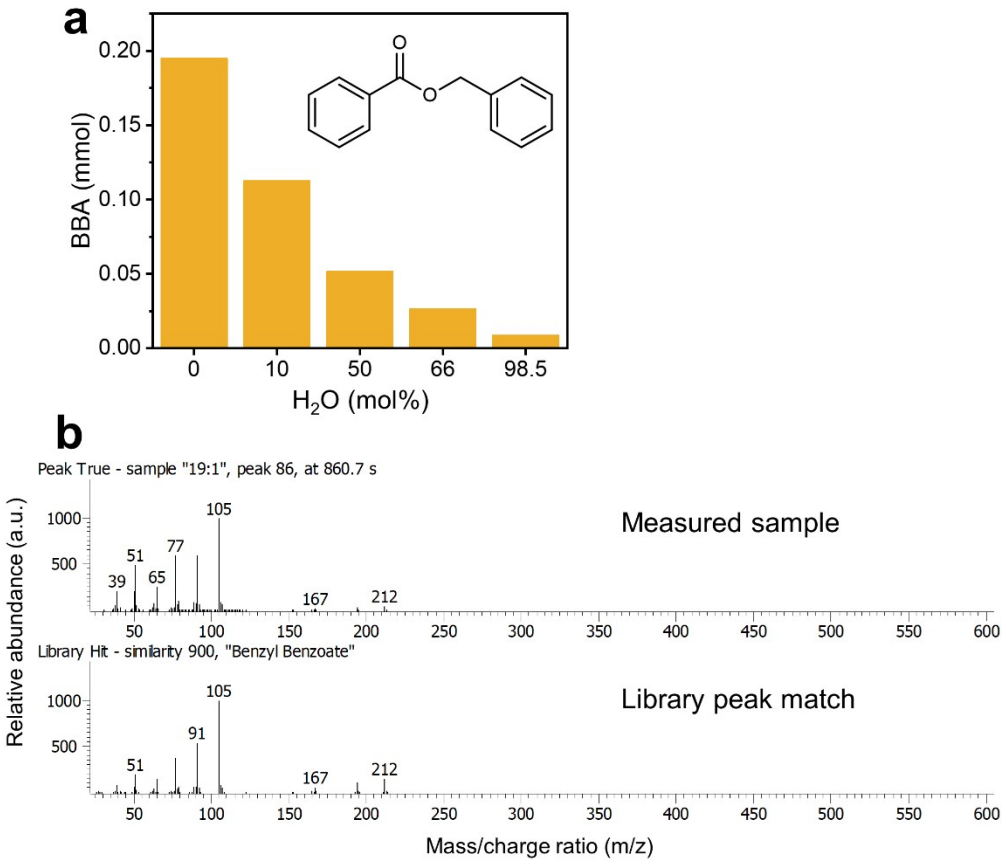

Fig. S13. Photocatalytic H_2 evolution in the organic working solution with CTF-Ph photocatalyst. Reaction condition: photocatalyst (30 mg), organic working solutions (30 mL), AM 1.5G simulated sunlight (~890 W m^{-2}), 3 h, He (saturated), 298 K.

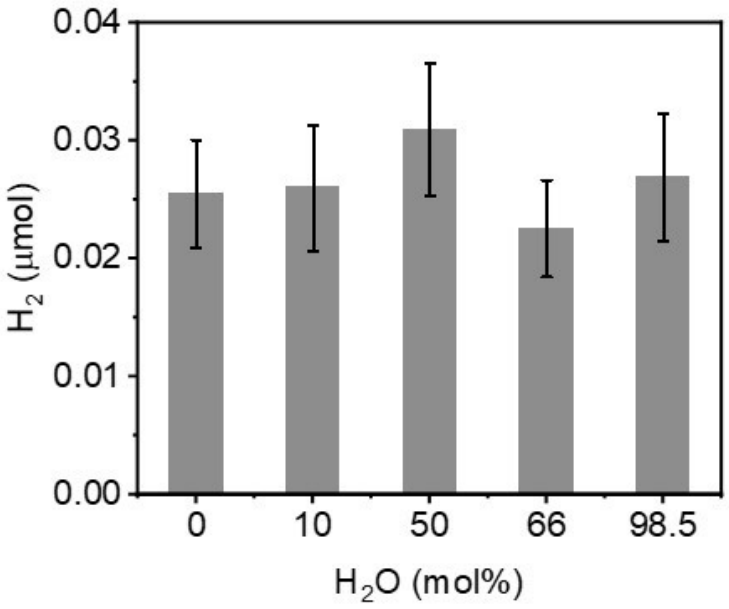

Fig. S14. Electron paramagnetic resonance (EPR) spectra for BLK, CTF-Ph, and TiO_2 in 100% MeOH under simulated AM 1.5G solar light. Reaction condition: MeOH (3 mL), O_2 (purged for 30 min), 298 K, photocatalysts (10 mg), DMPO (20 μL), reaction time (60 min), reaction vessel volume (4 mL).

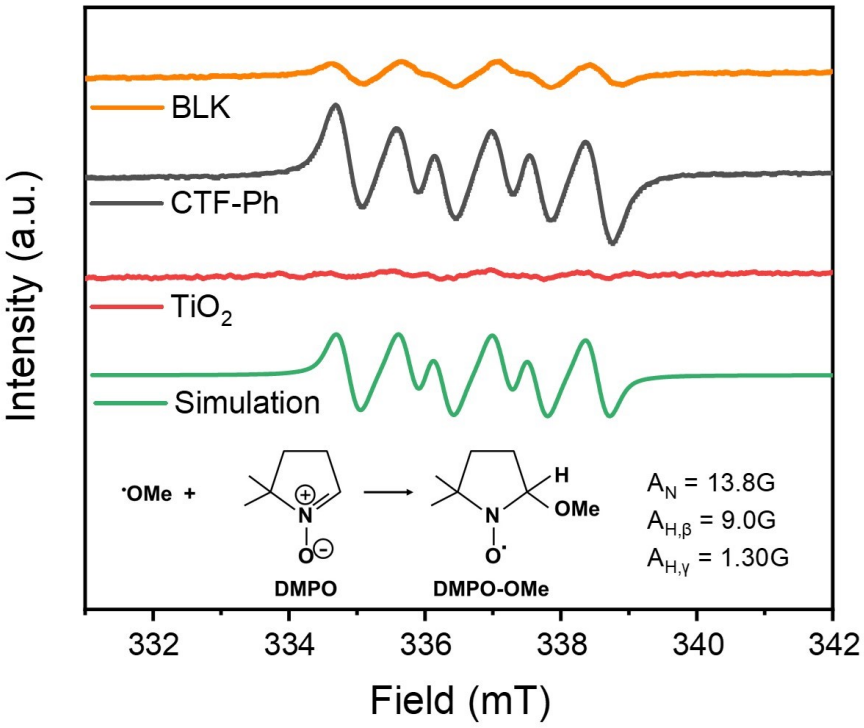

Note: After an hour of irradiation, six lines of EPR spectra were observed, and which was assigned to be DMPO-methoxyl (•OMe) adduct (g = 2.00561; A_N = 13.8 G; $A_{H,\beta}$ = 9.0 G; $A_{H,\gamma}$ = 1.30 G) and well matched with simulated spectrum by Easyspin software package (line width 3.2G; Lorenztian 80%). DMPO-methoxyl adduct were generated by oxidation of methanol, and the formation of methoxyl radical were affected by the types of photocatalysts. In particular, the EPR intensity for CTF-Ph was much higher than that of BLK. This indicates that photo-generated charge separation on CTF-Ph is highly efficient, which in turn increases the H_2O_2 production by the photocatalytic O_2 reduction. Otherwise, generation of methoxyl radical was noticeably restrained by TiO_2 photocatalyst compared to BLK, which indicates negative contribution of TiO_2 in the reaction.

Fig. S15. Photocatalytic decomposition of H_2O_2 in (a) pure water and (b) organic working solution. Reaction condition: photocatalyst (20 mg), solution (10 mL; 100% water for aqueous condition and 50:50% BzOH:MeCN for organic condition), H_2O_2 (C_0 10 mM), Ar (1 bar), AM 1.5G simulated sunlight (~980 W m^{-2}), 298 K.

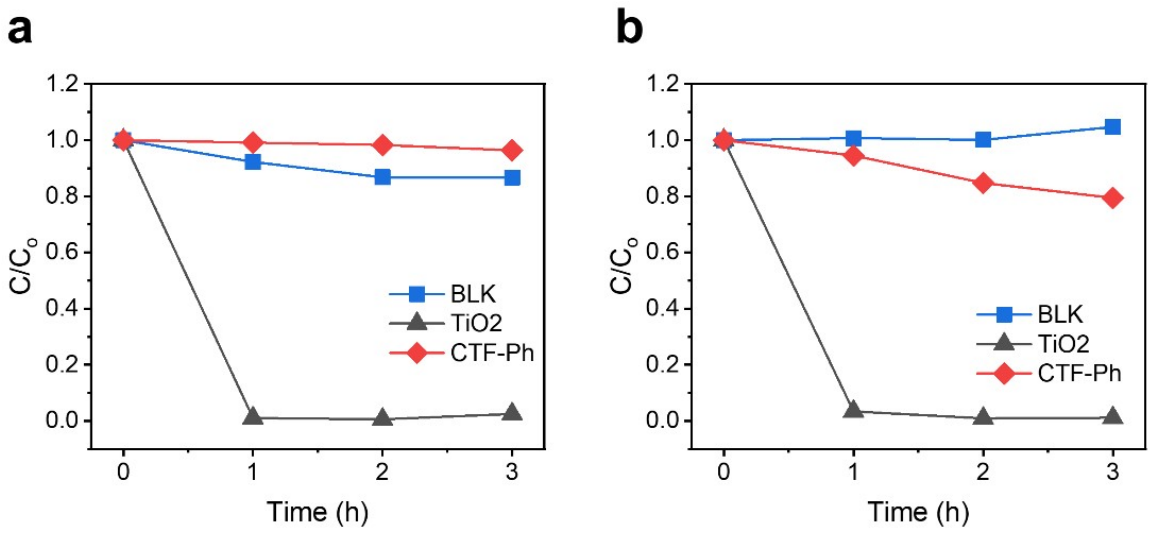

Fig. S16. EPR spectra of (a) DMPO-hydroxyl (•OH) and (b) DMPO-hydroperoxyl (•OOH) radicals from H_2O_2 decomposition with CTF-Ph, TiO_2, and BLK under simulated AM 1.5G light irradiation. Reaction condition for (a): water (3 mL), photocatalyst (10 mg), H_2O_2 (10 mM), Ar (purged for 30 min), 298 K, DMPO (20 µl); (b): BzOH (1.5 ml), acetonitrile (1.5 mL), H_2O_2 (10 mM), photocatalyst (10 mg), Ar (purged for 30 min), 298 K, DMPO (20 µl). EPR spectra were obtained both in dark and light conditions, where 0- and 15-min signals were obtained in dark, and 30-min data was taken after 15 min of light illumination.

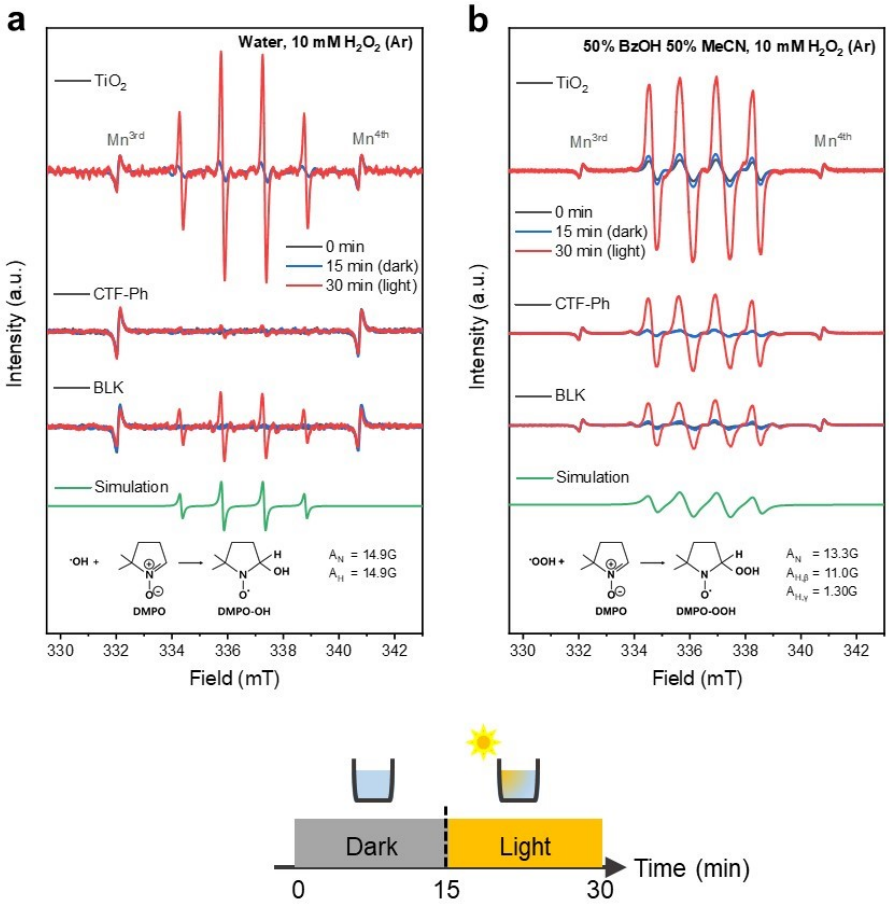

Note: In pure water under Ar condition, four lines of EPR spectra were observed with CTF-Ph, TiO_2, and BLK, assigned to be DMPO-•OH adduct (g = 2.00561; A_N = 14.9 G; A_H = 14.9 G) and well matched with the simulated spectrum by Easyspin software package (line width 3.0 G; Lorenztian 50%). On the other hand, in 50% BzOH under Ar condition, four lines of EPR spectra were evolved, assigned to be DMPO-•OOH adduct (g = 2.00561; A_N = 13.6 G; $A_{H,\beta}$ = 11.0 G; $A_{H,\gamma}$ = 1.30 G) and well corresponded to the simulated spectrum (line width 3.0 G; Lorenztian 80%). In both aqueous and organic conditions, the radicals generated from H_2O_2 decomposition were the most intense in the presence of TiO_2 compared to those of CTF-Ph and BLK. These results support the role of photocatalysts in producing and degrading H_2O_2 in the reaction media.

Fig. S17. (a) Metal-free polymeric photocatalysts commonly studied in heterogeneous photocatalysis. (b) Electronic band structures of the tested photocatalysts. (c) H_2O_2 and BzCHO formation in the organic working solutions using the polymeric photocatalysts. Reaction condition: photocatalyst (50 mg), organic working solution (30 mL, 50:50% BzOH:MeCN), AM 1.5G simulated sunlight (~980 W m^{-2}), O_2 (1 bar), 298 K.

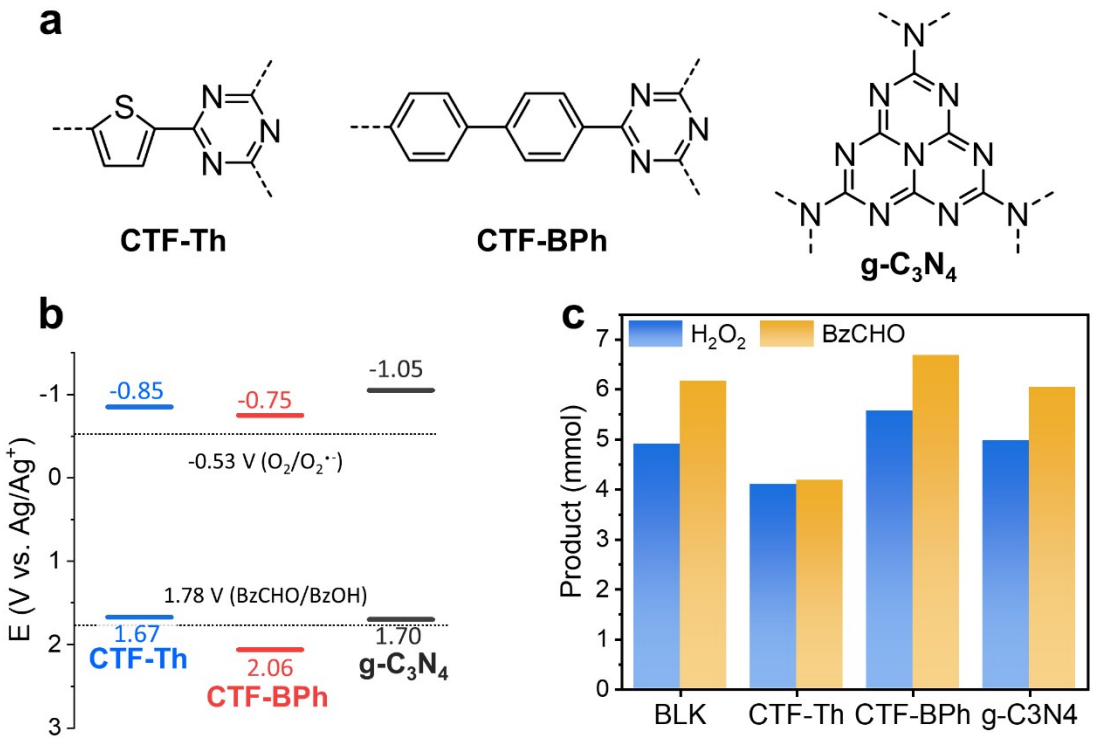

Note: Metal-free polymeric photocatalysts exhibited good H_2O_2 and BzCHO production efficiencies in the given organic working solutions. The oxidation potentials of CTF-Th, CTF-BPh, and g-C_3N_4 were less strong than that of CTF-Ph, showing relatively lower efficiency in H_2O_2 and BzCHO production. In these examples, H_2O_2 and BzCHO production efficiencies strongly depend on the redox potentials of the photocatalysts, which validates the fact that the photocatalyst plays a major role in these reactions.

Fig. S18. EPR spectra of DMPO-hydroxyl (•OH) with CTF-Ph under simulated AM 1.5G light irradiation. Reaction condition: water (3 mL), O_2 (purged for 30 min), CTF-Ph (30 mg), 298 K, DMPO (20 μl).

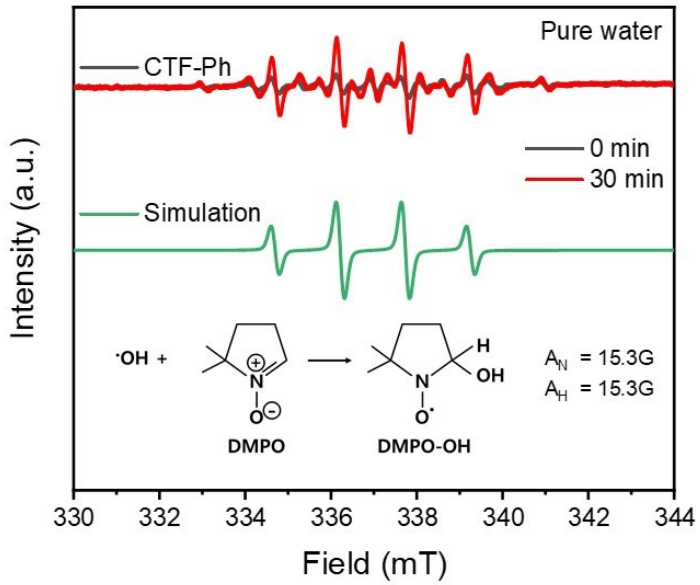

Note: In O_2-saturated pure water, four lines of strong EPR spectra were observed, which were assigned to be DMPO-•OH adduct (g = 2.00561; A_N = 15.3 G; A_H = 15.3 G) and well matched with the simulated spectrum by Easyspin software package (line width 1.7 G; Lorenztian 80%). The DMPO-•OH is generated with CTF-Ph photocatalyst in water since the photogenerated holes are scavenged by water oxidation reaction. However, •OH radical was scarcely detected in the OWS condition where the BzOH oxidation is superior to water oxidation, and the BzOH-abundant OWS condition produced the strong OR• radicals as the main signal.

Fig. S19. *In-situ* EPR spectra for (a) CTF-Ph and (b) BLK in organic working solution (50% BzOH, 50% MeCN, 0 mol% water) under simulated AM 1.5G light irradiation. Reaction condition: BzOH (50 μL), MeCN (50 μL), O_2 (purged for 30 min), 298 K, DMPO (1.33 μL), CTF-Ph (0.67 mg). EPR spectra were obtained every 1 min for 30 min.

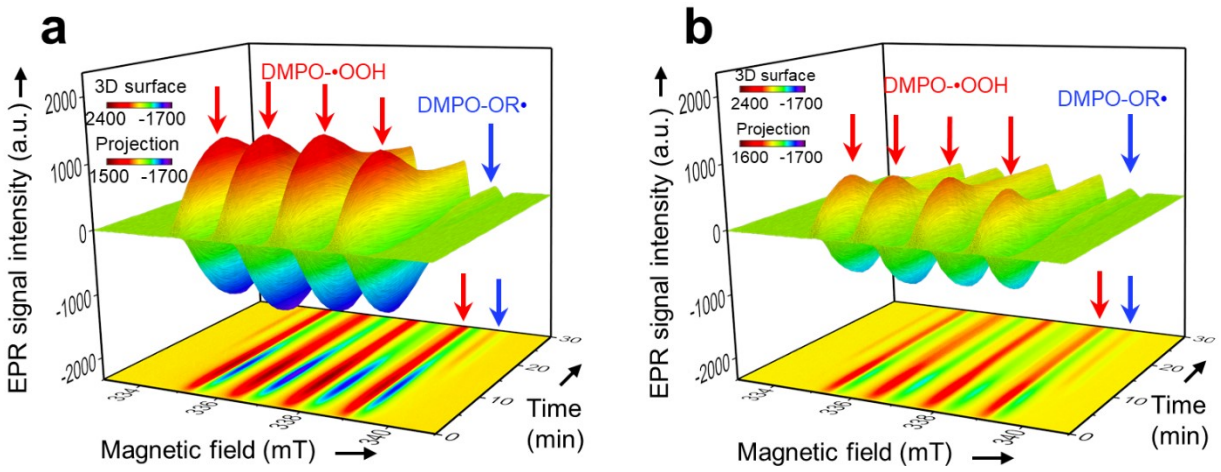

Fig. S20. UV-vis absorption spectra of (a) BzOH and (b) BzCHO solutions with concentrations from 0.1 M to 2.5 M in acetonitrile (MeCN).

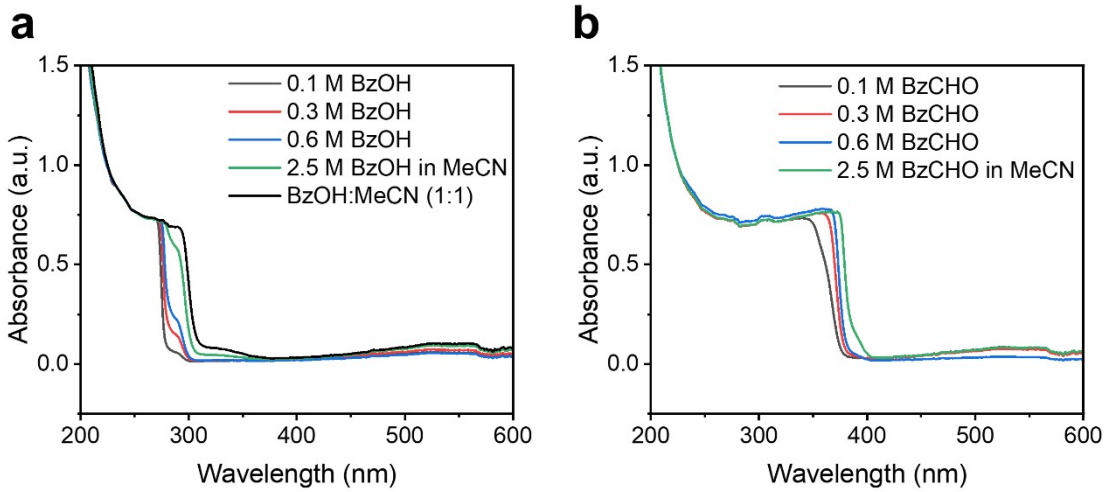

Fig. S21. (a) Concentration of BzCHO in pure BzOH sample determined by GC-MS spectrum. (b) H_2O_2, (c) BzCHO, and (d) BBA formation in the BLK solution with the intentionally spiked 0.005%, 0.01% and 0.1% of BzCHO from the beginning of the reaction. Reaction condition: Solution (10 mL; 50:50% BzOH:MeCN), AM 1.5G simulated sunlight (~980 W m^{-2}), O_2 (1 bar), 298 K.

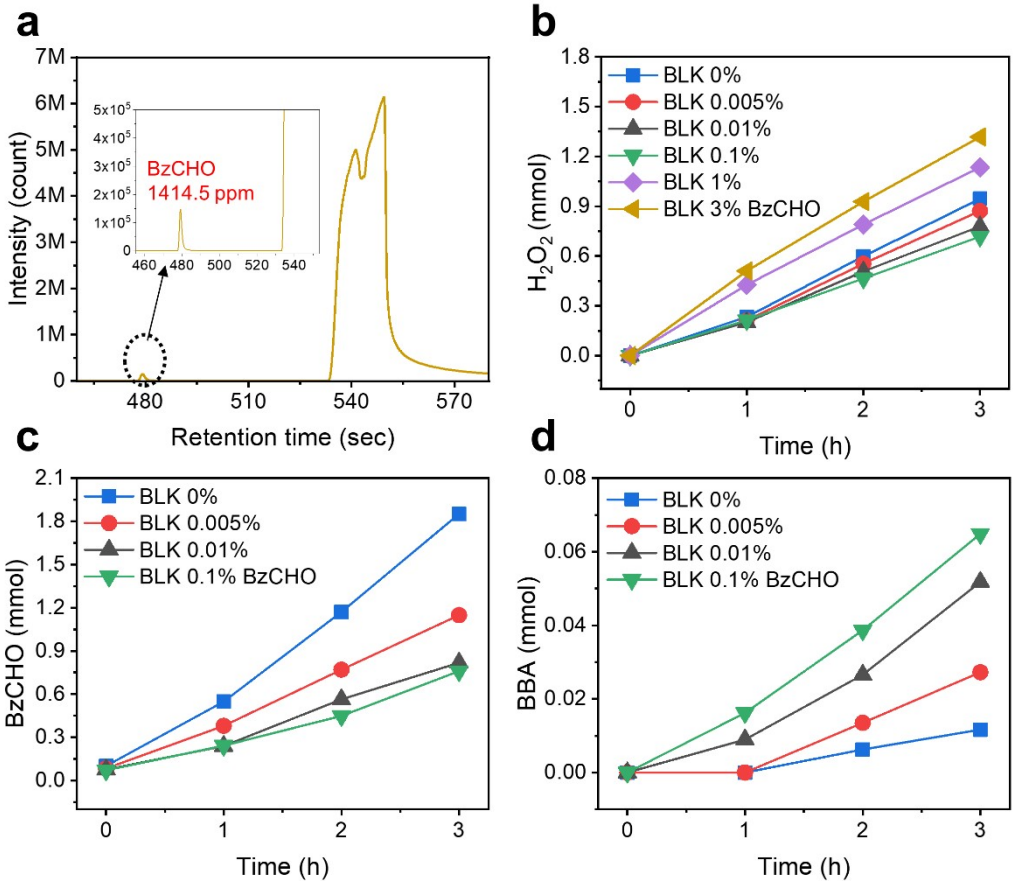

Note: (a) BzCHO exists in the pure BzOH solution (108006-1L supplied from Sigma Aldrich) up to 1414.5 ppm (in the average of triplicate measurements). (b-c) The addition of BzCHO in the BLK reactions hindered the formation of H_2O_2 and BzCHO. The formation of BBA was rather increased with respect to increasing the initial BzCHO contents. BBA is potentially generated by the coupling between benzoyl radical (light-initiated radical from BzCHO) and alkoxyl radical (photo-oxidized radical from BzOH, minor detected as shown in Fig. S22). A higher production of BBA with increasing BzCHO concentration resulted from the formation of benzoyl radical from photo-excited BzCHO. When BzCHO addition was in excess (>1%), H_2O_2 formation became higher than that from BLK without BzCHO addition, probably due to the stronger light absorbance with the excessive amount of BzCHO.

Fig. S22. EPR spectra of DMPO-alkoxyl (•OR) radical with CTF-Ph under white LED illumination (λ>400 nm). Reaction condition: BzOH (7.5 mL), MeCN (7.5 mL), O_2 (purged for 30 min), 298 K, DMPO (20 μL), photocatalyst (25 mg). EPR spectra were obtained after 30 min of LED irradiation.

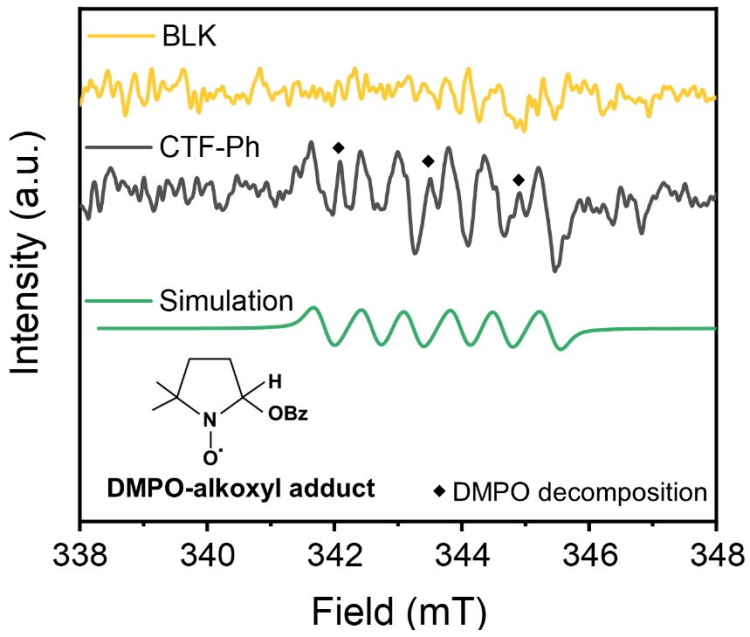

Note: From EPR data obtained after white LED irradiation, the formation of DMPO-alkoxyl radical was marginally observed [g = 2.00714; A_N = 14.0 G; $A_{H,\beta}$ = 7.4 G; $A_{H,\gamma}$ = 1.30 G]. Under the visible light >400 nm, the contribution of auto-oxidation to the reaction is fully removed and there was no peak evolved in BLK. This indicates that photo-oxidized alkoxyl radicals were also co-generated, although it was too minor to be detected under solar irradiation.

Fig. S23. (a) Fluorescence spectra of $Ru(bpy)_3^{2+}$ complex in the organic working solutions with different water contents (solid lines). Fluorescence quenching was observed by the addition of O_2 in the solution (dotted lines). (b) Fluorescence quenching of the Ru complex in the O_2-saturated water-organic mixtures.

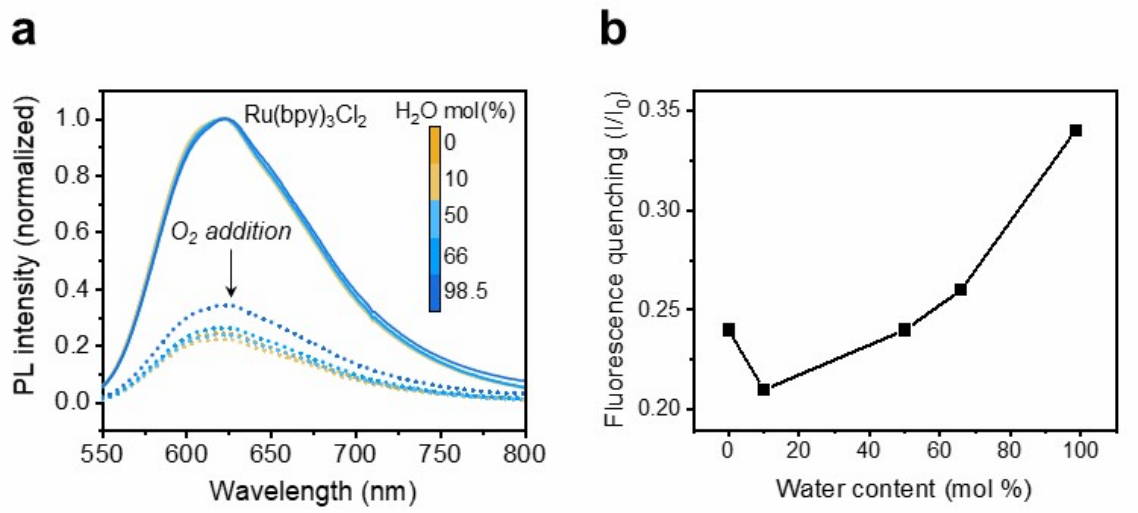

Note: (a) In principle, the O_2 solubility in organic solvent is far higher than that in aqueous solution[38]. The relative O_2 concentration in the organic solutions with the variation of water contents was measured by photochemical analysis with $Ru(bpy)_3^{2+}$ complex. The fluorescence quenching of the Ru complex by the response to O_2 can indicate the relative O_2 solubility in the given organic media. (b) The fluorescence quenching of Ru complex (I/I_0) was in the order of 10 mol% (0.21) > 0 mol% (0.24) = 50 mol% (0.24) > 66 mol% (0.26) > 98.5 mol% (0.34). The relative O_2 solubility was higher in the organic condition and further improved in the presence of a small quantity of water. The hydrogen bond between water and O_2 molecule in the organic solution can increase the O_2 solubility of the organic solvent up to 30%[38]. The higher O_2 dissolution in the organic working solution with a small portion of water can contribute to the photocatalytic O_2 reduction, eventually leading to enhanced H_2O_2 production.

Fig. S24. (a) Time-correlated single photon counting result of CTF-Ph in the given water/organic mixtures. (b) Estimated fluorescence lifetimes of CTF-Ph in water/organic mixtures.

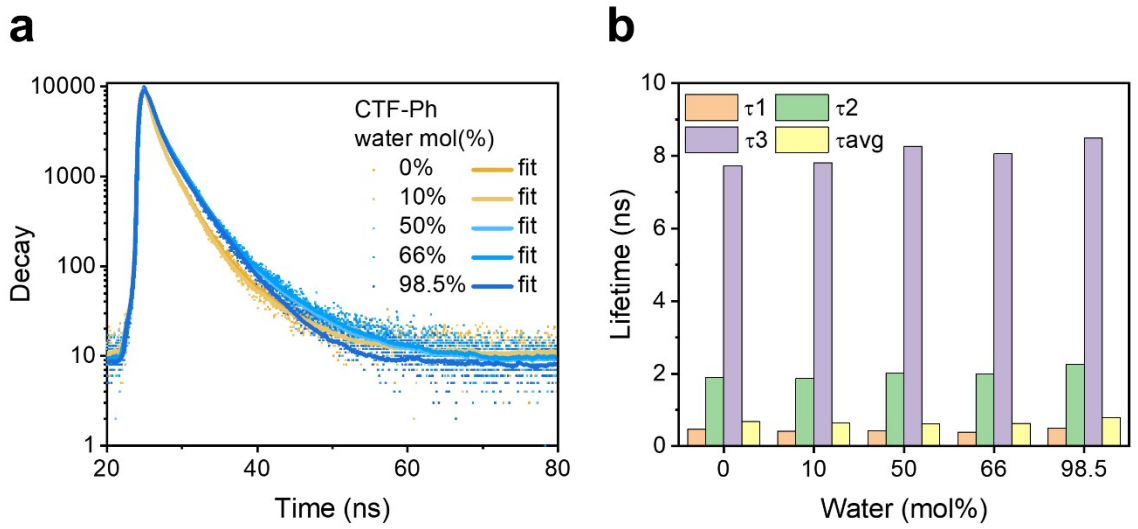

Note: The lifetime of the excited state in the organic working solutions was estimated using time-correlated single-photon counting. The average lifetimes of CTF-Ph were slightly shortened in the conditions with 0 to 50 mol% water in line with the static PL measurement.

Fig. S25. Average transmittance of CTF-Ph dispersions prepared in the given organic/water mixtures.

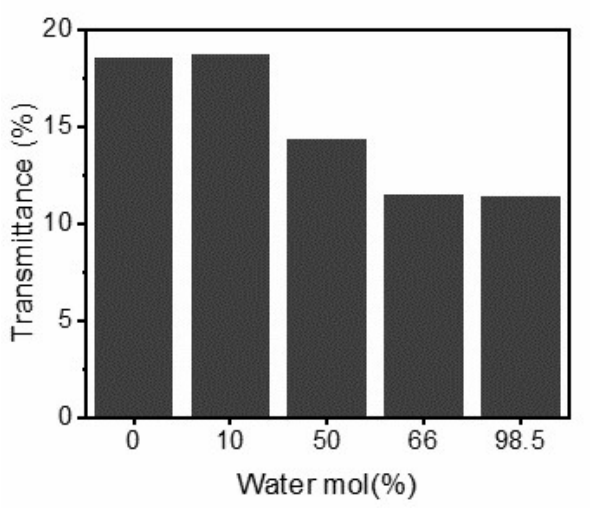

Fig. S26. ^{1}H NMR spectra of BzOH oxidation reactions with different amount of water in the system; (a) 3% mol H_2O, (b) 10% mol H_2O, and (c) 65% mol H_2O. (d) Stacked spectra of (a)~(c).

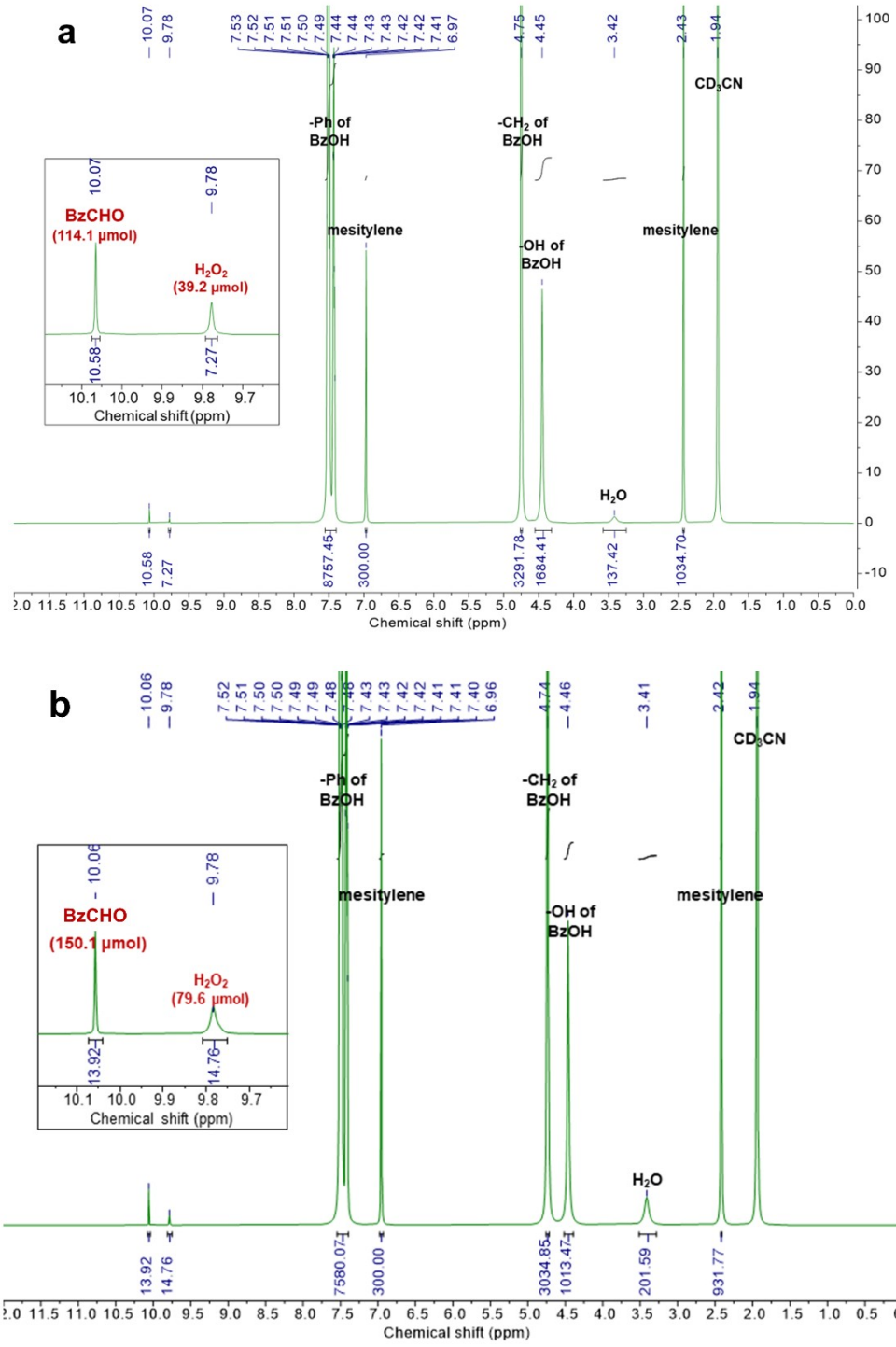

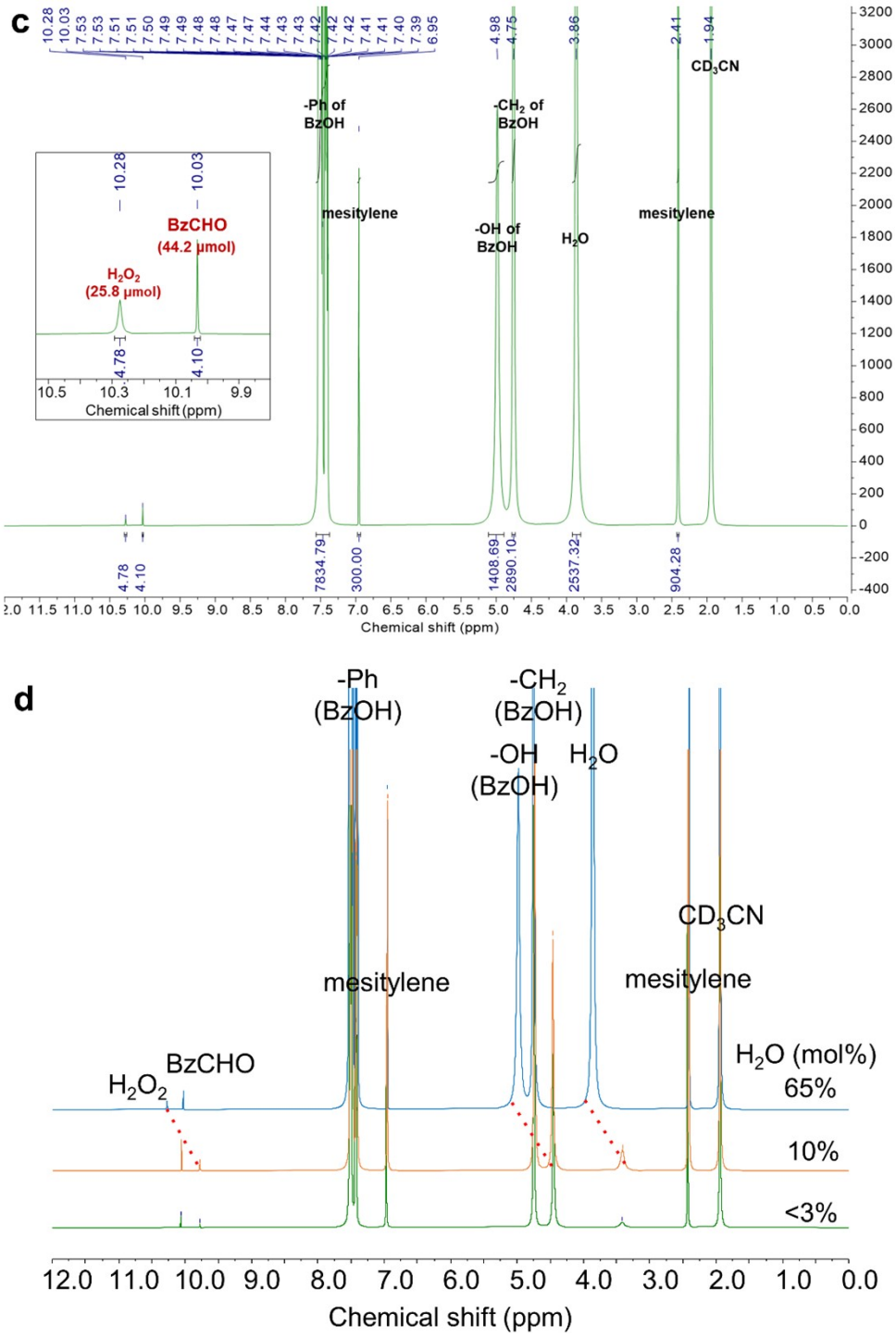

Note: The photo-oxidation facilitated by the addition of water could be also observed by ^{1}H NMR spectroscopy, where both BzCHO and H_2O_2 peaks became more significant at 10.06 and 9.87 ppm, respectively, when with the optimum dose of water (~10 mol% H_2O). Besides, the peaks from water and the hydroxyl group of BzOH were shifted downfield due to the formation of hydrogen bond between water and BzOH molecules[39]. We note that a fine control in water contents was difficult in small NMR tubes, thus only three variations were shown (i.e., 3, 10, and 65 mol% H_2O).

Fig. S27. (a) ^{1}H NMR spectrum of H_2O_2 solution obtained from the long-term reaction and purified through a RO membrane filtration (CD_3CN, 298 K). (b) Total organic carbon (TOC) and H_2O_2 concentrations of crude aqueous extract and purified samples before and after the membrane filtration respectively.

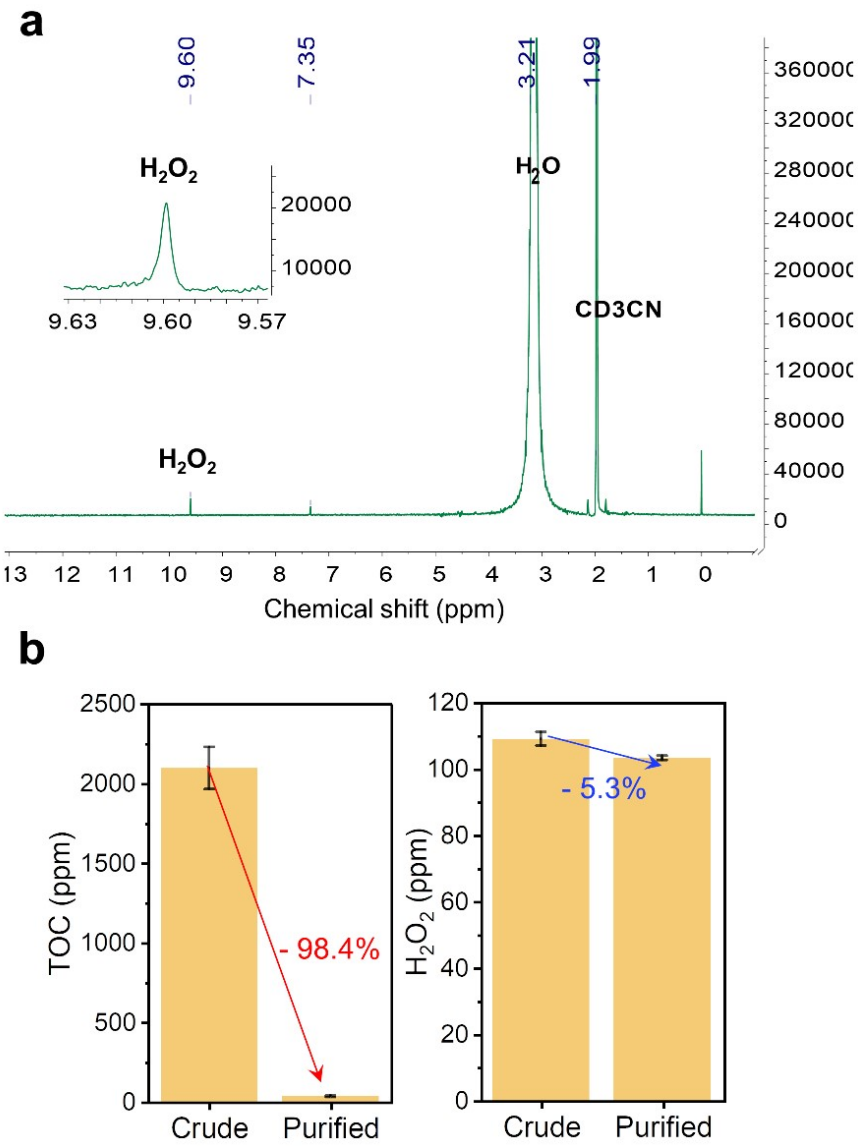

Fig. S28. (a) Solid-state ^{13}C CP-MAS NMR (*asterisk = satellite peak) and (b) FT-IR spectra of CTF-Ph before and after the long-term experiment.

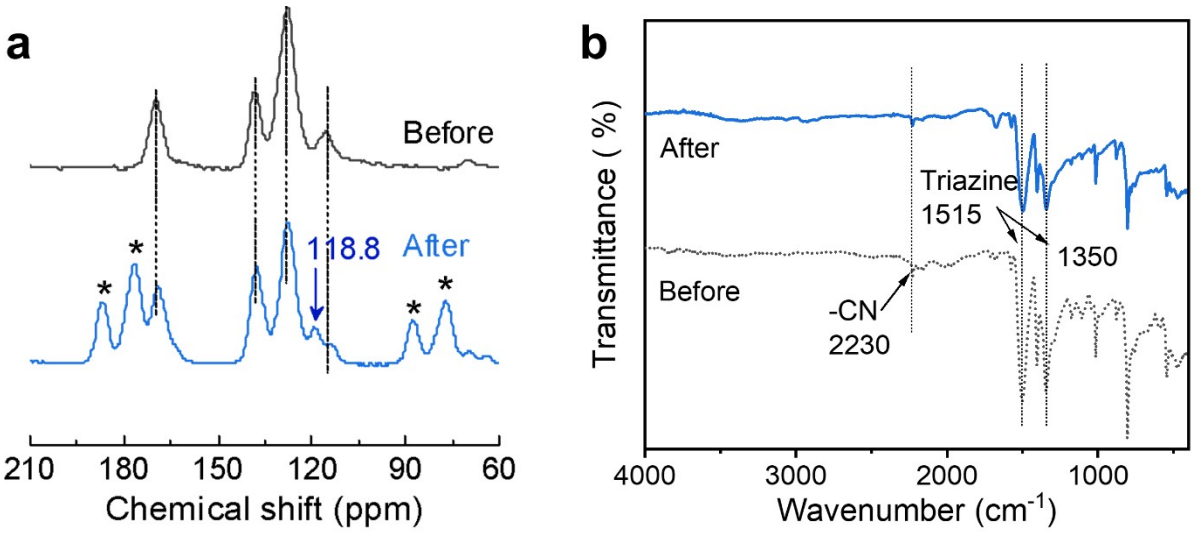

Note: (a) A slight peak evolved at 118.8 ppm after the long-term experiment is attributed to the addition of α-hydroxybenzyl radical on CTF-Ph.

Fig. S29. UV/vis diffuse reflectance spectra of CTF-Ph before and after the long-term experiment for 50 h. Inset shows the corresponding color change of the CTF-Ph powder.

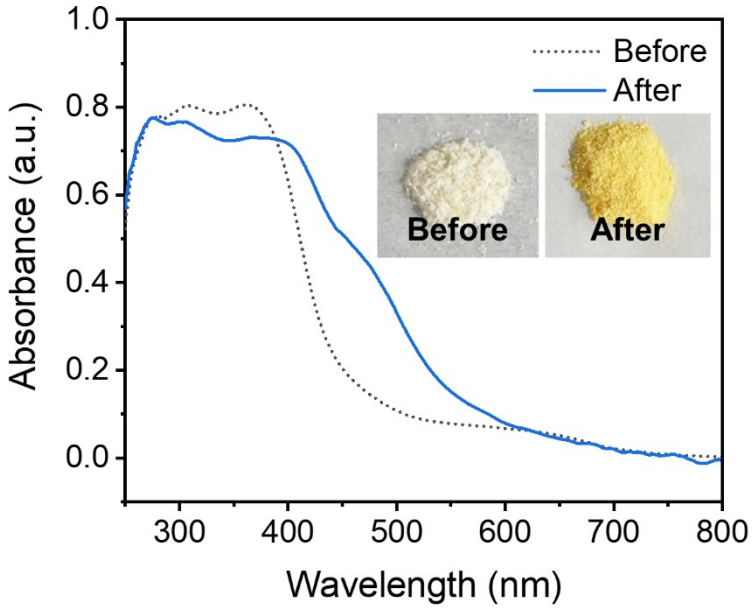

Fig. S30. Cyclic H_2O_2 production experiment with the organic working solution. Reaction condition: photocatalyst (50 mg), organic working solution (30 mL, 50:50% BzOH:MeCN), AM 1.5G simulated sunlight (~890 W m^{-2}), O_2 (1 bar), 298 K.

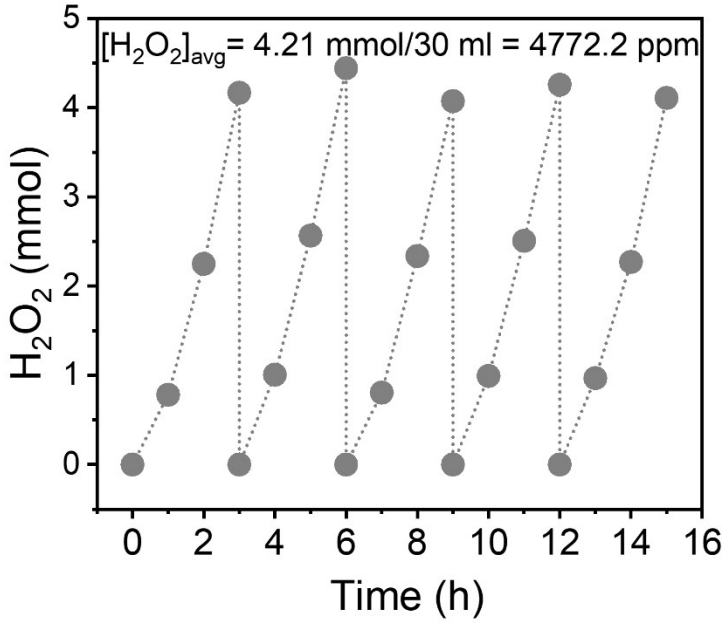

Fig. S31. Photograph of typical experimental set-up for photocatalytic H_2O_2 and BzCHO production in organic working solution.

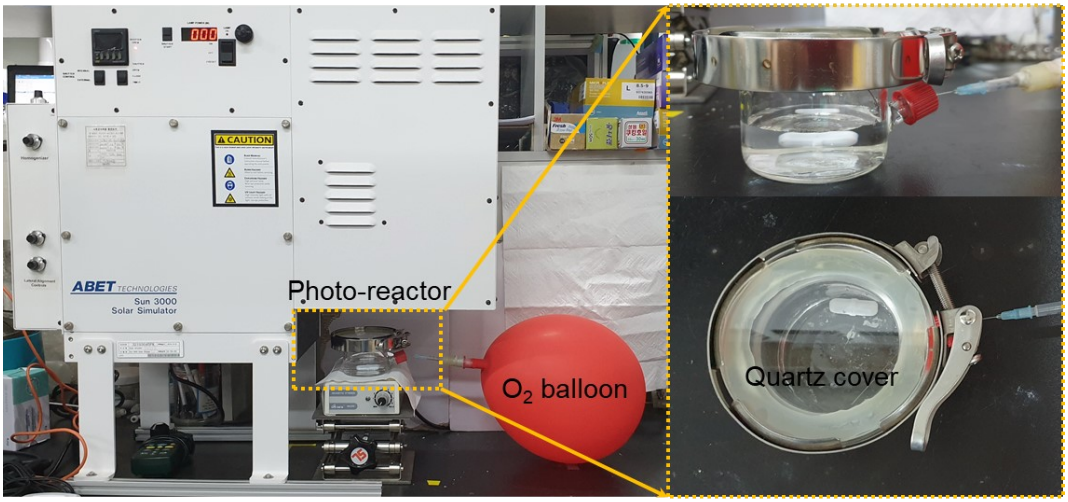

Fig. S32. Calibration curve for detection of H_2O_2 concentration using (a) titanium sulfate solution and (b) cerium sulfate solution.

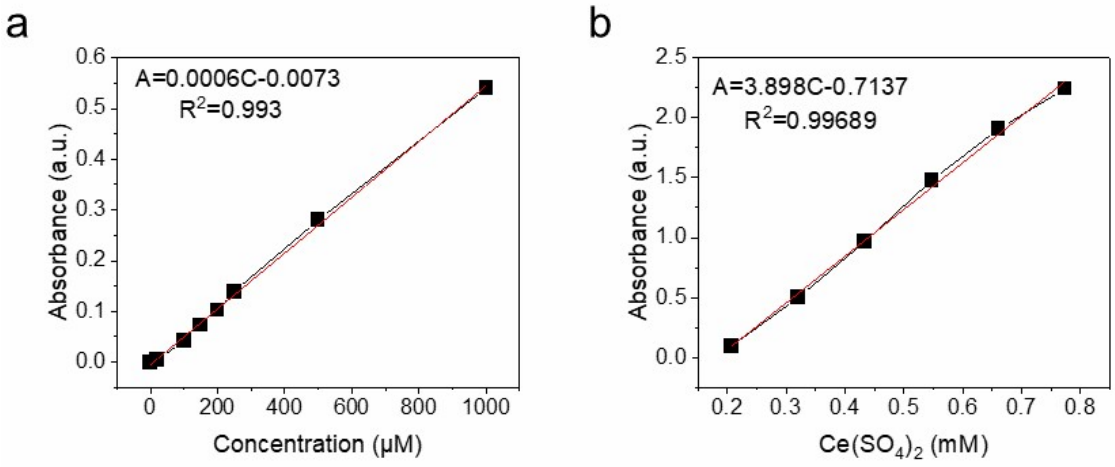

Fig. S33. Calibration curve for detection of BzCHO in organic working solution.

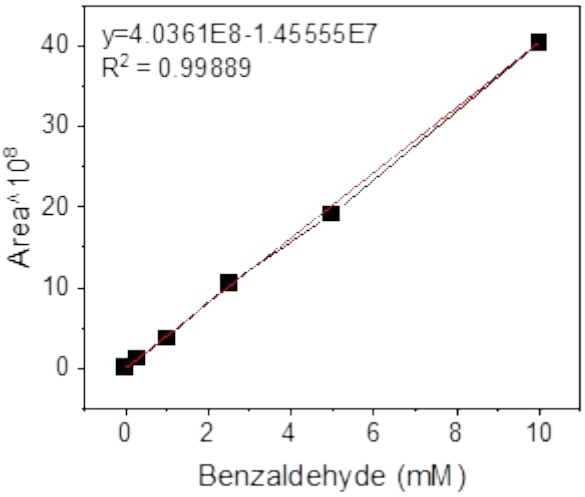

Fig. S34. Photograph of experimental set-up for *in-situ* EPR measurement.

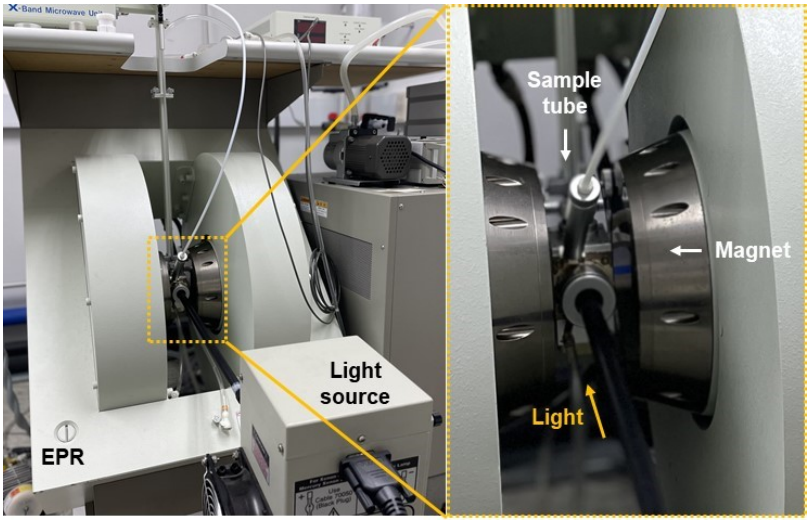

Fig. S35. SEM images of (a) mesoITO, (b,c) IO-ITO/mesoITO, and (d) CTF/IO-ITO/mesoITO photoelectrodes.

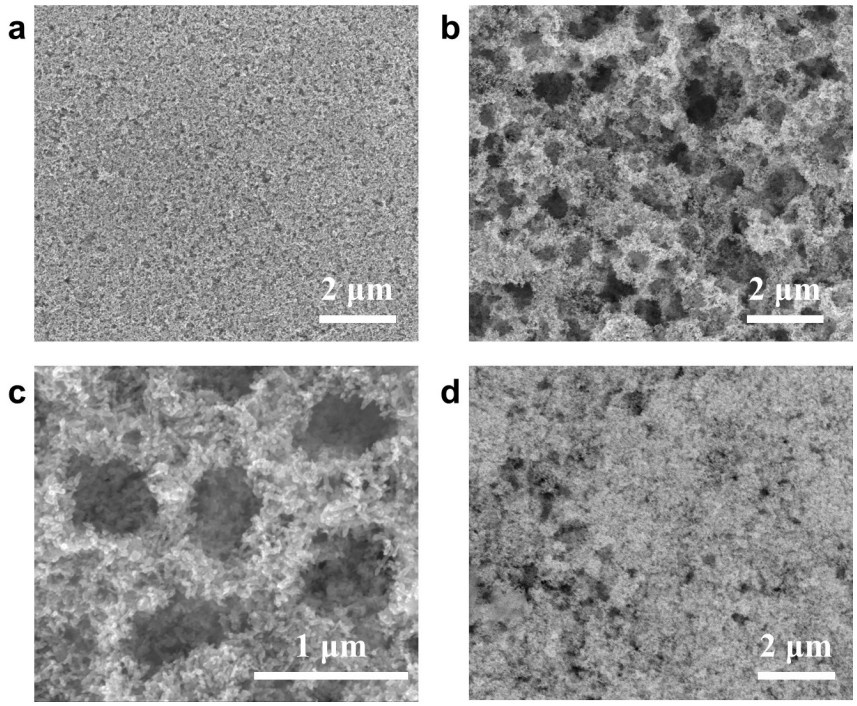

Note: The hierarchical structure of the IO-ITO/mesoITO electrode provides mesoporous and macroporous channels that enable facile loading of CTF catalysts on the electrode and penetration of reaction substrates.

Supplementary references

1. W. Huang, B. C. Ma, H. Lu, R. Li, L. Wang, K. Landfester and K. A. I. Zhang, *ACS Catal.*, 2017, **7**, 5438-5442.
2. G. Eisenberg, *Ind. Eng. Chem. Anal. Ed.*, 1943, **15**, 327-328.
3. L. Chen, L. Wang, Y. Wan, Y. Zhang, Z. Qi, X. Wu and H. Xu, *Adv. Mater.*, 2020, **32**, 1904433.
4. Y. Shiraishi, T. Takii, T. Hagi, S. Mori, Y. Kofuji, Y. Kitagawa, S. Tanaka, S. Ichikawa and T. Hirai, *Nat. Mater.*, 2019, **18**, 985-993.
5. S. Stoll and A. Schweiger, *J. Magn. Reson.*, 2006, **178**, 42-55.
6. M. Kato, T. Cardona, A. W. Rutherford and E. Reisner, *J. Am. Chem. Soc.*, 2013, **135**, 10610-10613.
7. Y. Shiraishi, S. Kanazawa, Y. Sugano, D. Tsukamoto, H. Sakamoto, S. Ichikawa and T. Hirai, *ACS Catal.*, 2014, **4**, 774-780.
8. Y. Kofuji, Y. Isobe, Y. Shiraishi, H. Sakamoto, S. Tanaka, S. Ichikawa and T. Hirai, *J. Am. Chem. Soc.*, 2016, **138**, 10019-10025.
9. Y. Kofuji, Y. Isobe, Y. Shiraishi, H. Sakamoto, S. Ichikawa, S. Tanaka and T. Hirai, *ChemCatChem*, 2018, **10**, 2070-2077.
10. Y. Shiraishi, Y. Kofuji, H. Sakamoto, S. Tanaka, S. Ichikawa and T. Hirai, *ACS Catal.*, 2015, **5**, 3058-3066.
11. X. Zeng, Y. Liu, Y. Kang, Q. Li, Y. Xia, Y. Zhu, H. Hou, M. H. Uddin, T. R. Gengenbach, D. Xia, C. Sun, D. T. McCarthy, A. Deletic, J. Yu and X. Zhang, *ACS Catal.*, 2020, **10**, 3697-3706.
12. H. I. Kim, Y. Choi, S. Hu, W. Choi and J. H. Kim, *Appl Catal B-Environ*, 2018, **229**, 121-129.
13. C. Chu, Q. Zhu, Z. Pan, S. Gupta, D. Huang, Y. Du, S. Weon, Y. Wu, C. Muhich, E. Stavitski, K. Domen and J.-H. Kim, *Proc. Natl. Acad. Sci.*, 2020, **117**, 6376-6382.
14. Y. Fu, C. a. Liu, M. Zhang, C. Zhu, H. Li, H. Wang, Y. Song, H. Huang, Y. Liu and Z. Kang, *Adv. Energy Mater.*, 2018, **8**, 1802525.
15. Y. Yang, C. Zhang, D. L. Huang, G. M. Zeng, J. H. Huang, C. Lai, C. Y. Zhou, W. J. Wang, H. Guo, W. J. Xue, R. Deng, M. Cheng and W. P. Xiong, *Appl Catal B-Environ*, 2019, **245**, 87-99.
16. Y. X. Ye, C. Wen, J. H. Pan, J. W. Wang, Y. J. Tong, S. B. Wei, Z. F. Ke, L. Jiang, F. Zhu, N. B. Zhou, M. J. Zhou, J. Q. Xu and G. F. Ouyang, *Appl Catal B-Environ*, 2021, **285**.
17. Z. Wei, M. L. Liu, Z. J. Zhang, W. Q. Yao, H. W. Tan and Y. F. Zhu, *Energy Environ. Sci.*, 2018, **11**, 2581-2589.
18. L. Zhou, J. R. Feng, B. C. Qiu, Y. Zhou, J. Y. Lei, M. Y. Xing, L. Z. Wang, Y. B. Zhou, Y. D. Liu and J. L. Zhang, *Appl Catal B-Environ*, 2020, **267**.
19. Y. Isaka, Y. Kondo, Y. Kawase, Y. Kuwahara, K. Mori and H. Yamashita, *Chem. Commun.*, 2018, **54**, 9270-9273.
20. Y. Isaka, Y. Kawase, Y. Kuwahara, K. Mori and H. Yamashita, *Angew. Chem. Int. Ed.*, 2019, **58**, 5402-5406.
21. X. L. Chen, Y. Kuwahara, K. Mori, C. Louis and H. Yamashita, *J. Mater. Chem. A*, 2020, **8**, 1904-1910.
22. Y. Shiraishi, T. Takii, T. Hagi, S. Mori, Y. Kofuji, Y. Kitagawa, S. Tanaka, S.

Ichikawa and T. Hirai, *Nat. Mater.*, 2019, **18**, 985-993.
23. C. Krishnaraj, H. Sekhar Jena, L. Bourda, A. Laemont, P. Pachfule, J. Roeser, C. V. Chandran, S. Borgmans, S. M. J. Rogge, K. Leus, C. V. Stevens, J. A. Martens, V. Van Speybroeck, E. Breynaert, A. Thomas and P. Van Der Voort, *J. Am. Chem. Soc.*, 2020, **142**, 20107-20116.
24. Z.-A. Lan, M. Wu, Z. Fang, X. Chi, X. Chen, Y. Zhang and X. Wang, *Angew. Chem. Int. Ed.*, 2021, **60**, 16355-16359.
25. L. Liu, M.-Y. Gao, H. Yang, X. Wang, X. Li and A. I. Cooper, *J. Am. Chem. Soc.*, 2021, **143**, 19287–19293.
26. X. Zhang, P. Ma, C. Wang, L. Gan, X. Chen, P. Zhang, Y. Wang, H. Li, L. Wang, X. Zhou and K. Zheng, *Energy Environ. Sci.*, 2022, **15**, 830-842.
27. P. Zhang, Y. Tong, Y. Liu, J. J. M. Vequizo, H. Sun, C. Yang, A. Yamakata, F. Fan, W. Lin, X. Wang and W. Choi, *Angew. Chem. Int. Ed.*, 2020, **59**, 16209-16217.
28. Z. Teng, Q. Zhang, H. Yang, K. Kato, W. Yang, Y.-R. Lu, S. Liu, C. Wang, A. Yamakata, C. Su, B. Liu and T. Ohno, *Nat. Catal.*, 2021, **4**, 374-384.
29. S. Wang, B. Cai and H. Tian, *Angew. Chem. Int. Ed.*, 2022, **61**, e202202733.
30. K. H. Kim, S. J. Kim, W. H. Choi, H. Lee, B. C. Moon, G. H. Kim, J. W. Choi, D. G. Park, J. H. Choi, H. Kim and J. K. Kang, *Adv. Energy Mater.*, 2022, **12**, 2104052.
31. C. Xia, Y. Xia, P. Zhu, L. Fan and H. Wang, *Science*, 2019, **366**, 226-231.
32. E. Jung, H. Shin, B.-H. Lee, V. Efremov, S. Lee, H. S. Lee, J. Kim, W. Hooch Antink, S. Park, K.-S. Lee, S.-P. Cho, J. S. Yoo, Y.-E. Sung and T. Hyeon, *Nat. Mater.*, 2020, **19**, 436-442.
33. W. Li, A. Bonakdarpour, E. Gyenge and D. P. Wilkinson, *ChemSusChem*, 2013, **6**, 2137-2143.
34. X. Zhang, X. Zhao, P. Zhu, Z. Adler, Z.-Y. Wu, Y. Liu and H. Wang, *Nat. Commun.*, 2022, **13**, 1-11.
35. Q. Chang, P. Zhang, A. H. B. Mostaghimi, X. Zhao, S. R. Denny, J. H. Lee, H. Gao, Y. Zhang, H. L. Xin and S. Siahrostami, *Nat. Commun.*, 2020, **11**, 1-9.
36. T. Chen, W.-Q. Li, W.-B. Hu, W.-J. Hu, Y. A. Liu, H. Yang and K. Wen, *RSC Adv.*, 2019, **9**, 18008-18012.
37. M. J. Berr, P. Wagner, S. Fischbach, A. Vaneski, J. Schneider, A. S. Susha, A. L. Rogach, F. Jäckel and J. Feldmann, *Appl. Phys. Lett.*, 2012, **100**, 223903.
38. Q. Li, C. Batchelor-McAuley, N. S. Lawrence, R. S. Hartshorne and R. G. Compton, *J. Electroanal. Chem.*, 2013, **688**, 328-335.
39. M. Liu, Z. Zhang, H. Liu, Z. Xie, Q. Mei and B. Han, *Sci. Adv.*, 2018, **4**, eaas9319.